

Aerodynamic Characteristics of Bodies of Revolution at Near-Sonic Speeds

Brenda M. Kulfan,* John E. Bussoletti,† and Craig L. Hilmes‡
The Boeing Company, Seattle, Washington 98124

DOI: 10.2514/1.30028

Recent near-sonic and low-sonic boom transport aircraft development studies have sparked a renewed interest in the nature of the aerodynamics about configurations at near-sonic or low-supersonic speeds. The validity of the wind-tunnel test facilities and the computational methods are challenged by the flow characteristics at near-sonic speeds. Fundamental aerodynamic studies were conducted to assess the ability of the TRANAIR full potential code to predict pressure distributions, drag, and flow characteristics around a family of sting-mounted truncated parabolic bodies of revolution at near-sonic and low-supersonic speeds by comparisons with an extensive existing wind-tunnel database. The analyses included both inviscid and viscous coupled boundary layer analyses. The investigations also included assessments of wind-tunnel wall interference effects as influenced by the various body geometries and test conditions. Extensive test versus theory comparisons of surface pressure distributions, flowfield pressures, and drag forces are presented for subsonic through low-supersonic Mach numbers for the family of test configurations. An additional objective of these studies was to demonstrate the value of using existing and even rather historic experimental data. The experimental data used in the current studies were obtained from NACA wind-tunnel tests reported in 1958.

Introduction

RECENT near-sonic and low-sonic boom transport aircraft development studies have sparked a renewed interest in the nature of the aerodynamics about configurations designed to cruise at near-sonic or low-supersonic speeds. The validity of both the wind-tunnel test facilities and the computational methods are challenged by the characteristics of the flow at near-sonic speeds. The flow disturbances induced by a configuration at near-sonic and low-supersonic speeds extend to very large lateral distances. This presents a significant challenge to obtain interference-free wind-tunnel test data and also greatly increases the required lateral extent of the typical computational domain.

Consequently, a number of fundamental aerodynamic studies were conducted to assess the ability of the TRANAIR full potential code to predict pressure distributions, drag, and flow characteristics around a family of sting-mounted truncated parabolic bodies of revolution at near-sonic and low-supersonic speeds by comparisons with an extensive existing wind-tunnel data base [1,2]. The analyses included both inviscid and viscous coupled boundary layer analyses. The investigations also included assessments of the effects of wind-tunnel wall interference as influenced by the various body geometries and test conditions.

The physics of the actual flow characteristics separating behind a truncated body and flowing onto a support sting are not correctly modeled by inviscid computational fluid dynamics (CFD) methods which typically include a constant area wake equal to the base area

that trails behind the body. Using an analogy between the separated flow from the aft body to the sting and that of separated flow behind a backward facing step, a simple representation of the wake shape was developed and implemented in the TRANAIR analyses.

The total drag for each configuration included the pressure drag obtained by integration of the pressure distributions, plus the viscous drag. For the inviscid analyses, the viscous drag was estimated by using flat plate skin friction theory. The viscous drag estimates for the coupled boundary layer viscous analyses were obtained by integration of the calculated local skin friction distribution over the surface area of each body.

This report presents the results of the subsonic, near-sonic, and supersonic investigations. An additional objective of these studies was to demonstrate the value of using existing and even rather historic experimental data. The experimental data used in the current studies were obtained from NACA wind-tunnel tests reported in 1958.

The study reported in this paper illustrates a process of using the essential tools of the aerodynamist shown in Fig. 1. These tools include computational fluid dynamics (CFD), experimental fluid dynamics (EFD), simplified fluid dynamics (SFD), visual fluid dynamics (VFD), and the most important tool of all, understanding fluid dynamics (UFD).

Bodies of Revolution at Near-Sonic Speeds

The flow about bodies of revolution has added significance at near-sonic and low-supersonic speeds because of the transonic equivalence rule first attributed [3] to Oswatitsch and Keune. The transonic equivalence rule states that the flow about a general “slender” configuration can be separated into two distinct parts which are simply added together algebraically to yield the total flowfield. One part can be thought of as the flow due to the local cross-sectional geometry shape of the configuration, and the other part as a mean flow imparted by remote parts of the configuration.

According to the transonic equivalence rule, the flow far away from a general slender configuration becomes axisymmetric and equal to the flow around an equivalent equal cross-sectional area body of revolution. Furthermore, the drag rise of an entire properly designed aircraft configuration at its design lift coefficient is equal to the drag of the equivalent body of revolution providing that the wing does not become prematurely critical in the flowfield induced by the equivalent body [4–6].

Presented as Paper 0684 at the 45th AIAA Aerospace Sciences Meeting and Exhibit, Grand Sierra Resort, Reno, Nevada, 8–11 January 2007; received 25 January 2007; accepted for publication 3 April 2007. Copyright © 2007 by The Boeing Company. Published by the American Institute of Aeronautics and Astronautics, Inc., with permission. Copies of this paper may be made for personal or internal use, on condition that the copier pay the \$10.00 per-copy fee to the Copyright Clearance Center, Inc., 222 Rosewood Drive, Danvers, MA 01923; include the code 0021-8669/07 \$10.00 in correspondence with the CCC.

*Engineer/Scientist–Technical Fellow, Enabling Technology and Research, Commercial Airplane Group, PO Box 3707, Seattle, WA 98124, Mail Stop 67-LF. AIAA Member.

†Engineer/Scientist, Enabling Technology and Research, Commercial Airplane Group, PO Box 3707, Seattle, WA 98124, Mail Stop 67-LF.

‡Engineering Applications Programmer, Information Technology, Commercial Airplane Group, PO Box 3707, Seattle, WA 98124, Mail Stop 67-LF.

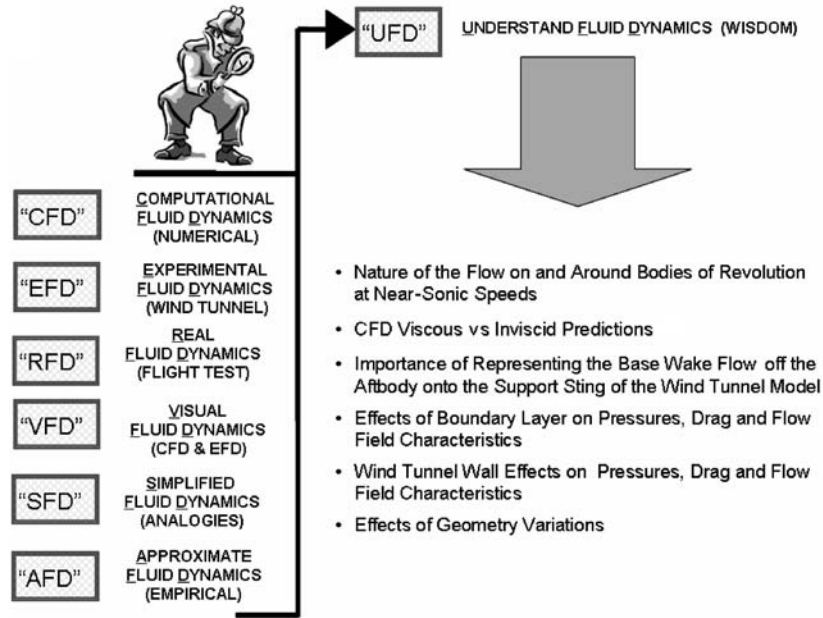


Fig. 1 Tools of the aerodynamicist.

Examples of applications of the equivalent body concept to complete transonic transport studies are shown in Fig. 2. Boeing early wind-tunnel tests results for a near-sonic transport wing-body combination [5] are shown in Fig. 2a. The incremental drag rise above Mach 0.8 is compared with the corresponding drag for the axisymmetric equivalent body. The drag rise characteristics are essentially equal even though the wing body is at the lift coefficient appropriate for cruise and the equivalent body is at zero angle of attack.

Figure 2b shows the application of the equivalent body area rule concept to a complete near-sonic configuration [6]. The shape of the total combined area plot is seen to be completely smooth thus delaying the appearance of the configuration shock and the associated drag rise to near-sonic speeds. The actual area is somewhat smaller than the total area in the vicinity of the wing to provide compensation for the wing lift. The lift compensation in the original form was put forth by R. T. Whitcomb for applications to configurations operating at near-sonic speeds. The fundamental design philosophy applied to these prior near-sonic configuration design activities was to develop a supercritical wing using the most

advanced airfoils and then using the equivalent body concept to develop a completely integrated configuration. The success of this approach is illustrated in the drag rise chart on the lower right which compares the drag rise of the of the near-sonic wing-body configuration with the corresponding axisymmetric equivalent body drag.

The transonic equivalence rule can also provide valuable insights into the nature of transonic flow about an aircraft, as well as about the desirable design features of transonic configurations.

Parabolic Bodies of Revolution Wind-Tunnel Database (Experimental Fluid Dynamics)

The experimental database used in the current study was obtained from published results of extensive systematic wind-tunnel test programs [1,2] that were conducted in the NASA Ames Research Center's 14 ft transonic wind tunnel. This tunnel had a closed-return circuit with a perforated test section with a porosity factor of 0.054 that permitted continuous operation from subsonic to low supersonic speeds. The wind-tunnel models, as shown in Fig. 3, included a

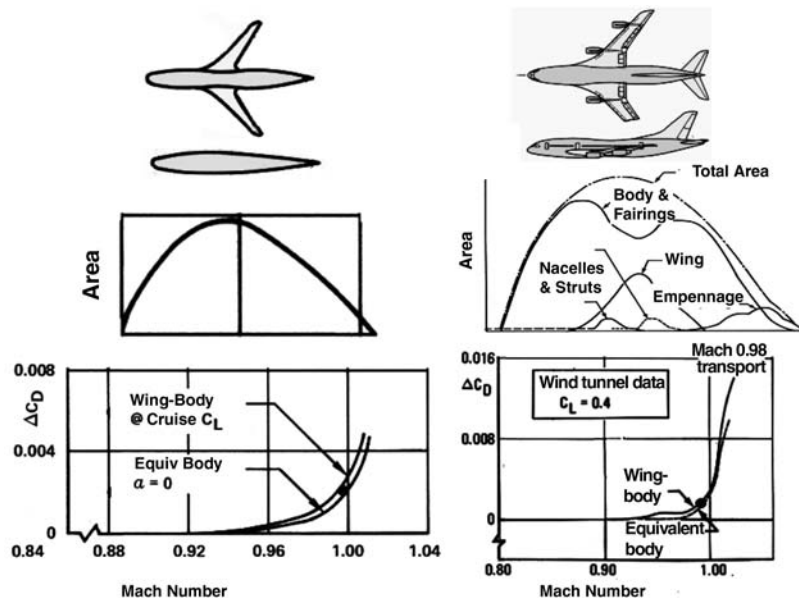


Fig. 2 Boeing wind-tunnel test validations of the equivalent body concept.

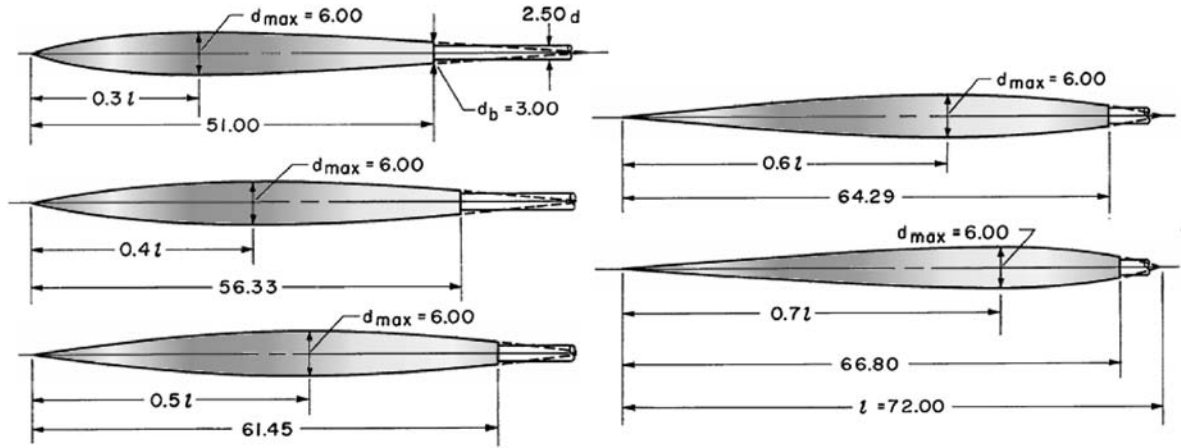


Fig. 3 Experimental parabolic bodies of revolution.

family of bodies of revolution having differing locations of the maximum cross-sectional area station that included 30, 40, 50, 60, and 70% of the total theoretical body length.

All the bodies had a fineness ratio of 12. The fineness ratio is defined as the ratio of the total body length L of 72 in. (from the nose to the theoretical point of closure) to the maximum diameter of the body of 6 in.

All the tested bodies were truncated to permit mounting on a sting supporting an internal force balance. The base area in all cases was equal to 25% of the maximum cross-sectional area which resulted in different lengths for each tested body.

The radius distribution for the 30 and 40% bodies were described by the equation

$$\frac{r(\xi)}{L} = \frac{R \max}{L} K1 \cdot [1 - \xi - (1 - \xi)^N] \quad (1)$$

The radius distribution for the 50, 60, and 70% bodies were described by the equation

$$\frac{r(\xi)}{L} = \frac{R \max}{L} K1 \cdot [\xi - \xi^N] \quad (2)$$

where $\xi = x/L$ is the nondimensional length ratio, $r(\xi)$ is the radius at station ξ , L is the theoretical overall body length (72 in.), $R \max$ is the maximum radius (6 in.), and $K1$ and N are defining constants as given in Table 1.

The wind-tunnel measurements included total force balance measurements, surface pressure measurements, and streamwise pressure measurements in the flowfield at a number of different radial distances from the bodies.

The complete set of the wind-tunnel test measurements is summarized in Table 2.

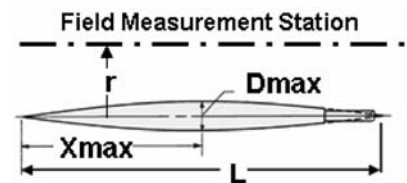
The extensive nature of this experimental test program is typical of the type of valuable fundamental research that was once the characteristic of NACA and early NASA research activities and

Table 1 Defining constants for the $R \max$ bodies

Body $R \max$ location	$K1$	N
30%	1.77	6.03
40%	2.36	3.39
50%	4.00	2.00
60%	2.36	3.39
70%	1.71	6.03

Table 2 Experimental database

Bodies $X \max / L$	Test Mach numbers	Force data	Radial location of off-body pressure measurements in max body diameters, $r/D \max$									
			Body CP	1	2	3	4	5	6	7	8	
30%	0.8	x	x	x	x	x	x	x	x	x	x	x
	0.9	x	x	x	x	x	x	x	x	x	x	x
	0.925	x	x	—	x	—	—	—	—	—	—	—
	0.95	x	x	x	x	x	x	—	—	—	—	—
	0.925	x	x	x	x	x	x	—	—	—	—	—
	1	x	x	x	x	x	x	x	x	x	x	x
	1.025	x	x	x	x	x	—	—	—	—	—	—
	1.05	x	x	x	x	x	x	—	—	—	—	—
	1.075	x	x	—	x	—	—	—	—	—	—	—
	1.1	x	x	x	x	x	x	x	x	x	x	x
40%	1.15	x	x	—	x	—	—	—	—	—	—	—
	1.2	x	x	x	x	x	x	x	x	x	x	x
	0.8	x	x	x	x	x	x	—	—	—	—	—
	0.9	x	x	x	x	x	x	—	—	—	—	—
	0.925	x	x	—	x	—	—	—	—	—	—	—
	0.95	x	x	x	x	x	x	—	—	—	—	—
	0.975	x	x	x	x	x	x	—	—	—	—	—
	1	x	x	x	x	x	x	—	—	—	—	—
	1.025	x	x	x	x	x	x	—	—	—	—	—
	1.05	x	x	x	x	x	x	—	—	—	—	—
60%	1.075	x	x	—	x	—	—	—	—	—	—	—
	1.1	x	x	x	x	x	x	—	—	—	—	—
	1.15	x	x	—	x	—	—	—	—	—	—	—
	1.2	x	x	x	x	x	x	—	—	—	—	—



occasionally that of previous industry-funded fundamental research activities. This type of fundamental research is essentially nonexistent in NASA and U.S. industry current “program-focused” aeronautics applied research activities. Consequently, unique sets of existing quality experimental data, such as being used in the current study, are extremely valuable to identify, retain, restore, and use.

TRANAIR Full Potential Flow Program (CFD)

The TRANAIR full potential flow program [7,8] was used to compute the surface pressure distributions on the body surfaces and in the flowfield about the models shown in Fig. 3. The analyses included inviscid analyses and coupled boundary analyses, both with and without simulation of the porous wind-tunnel walls. The wind-tunnel walls were simulated as though the wind tunnel had an axisymmetric circular porous test section. Consequently, the analytic representation is only an approximation to the actual rectangular test section. However if both the porous wall wind-tunnel test section and the analytical porous wall test section truly represented the desired free-air condition, the analytical free-air and porous wall predictions and the experimental test results would all be equal.

The TRANAIR computer program calculates the flow characteristics on and about arbitrary configurations at subsonic, transonic, and supersonic freestream Mach numbers. TRANAIR solves the nonlinear full potential equation subject to a variety of boundary conditions, modeling wakes, inlets, exhausts, porous walls, and impermeable surfaces. Viscous effects can be modeled using two different boundary layer codes. These include a finite difference boundary layer code, and an integral boundary layer code developed by Mark Drela [9,10]. Regions with different total temperature and pressure can be represented.

The TRANAIR program is used extensively in preliminary design and product development studies in the Boeing Commercial Aircraft Company particularly near cruise conditions. TRANAIR is an

extremely user-friendly and numerically efficient program with very fast analyses turn-around times, and was considered to be well suited for the current study. “In the spirit of Prandtl, Taylor, and von Karman, the conscientious engineer will strive to use as conceptually simple approach as possible to achieve his ends.” [11]

Initial Analyses and the Need to Model the Base Separation Wake (SFD)

Typical results of the initial analyses of the pressure distributions on the $X_{max}/L = 30\%$ body at a Mach number of 0.975 are shown in Fig. 4. The experimental data indicate the presence of a strong shock aft of the maximum body diameter station. The inviscid analysis predicted a very strong shock. The coupled boundary layer analysis softened the shock and more closely matched the test data. However, both the inviscid and the viscous analyses predicted a strong recovery in the pressures near the aft end of the wind-tunnel model which is not evident in the test data.

TRANAIR and other potential codes typically represent an open aft end body by a constant area wake extending downstream of the body (Fig. 5). This analysis model results in a discontinuous slope at the aft end of the body. This forces the pressure to rapidly recover at the aft end of the body. The recovery pressures, on the aft end of the body, create a local thrust force which nearly cancels the total body pressure drag force.

The actual flow over an aft body supported by a reduced area sting, however, is quite similar to the flow over the backward-facing step [12] shown in Fig. 6.

The flow separates behind the step and forms a region of trapped recirculating separated flow. The boundary layer forward of the step essentially flows over the dividing streamline, which divides the recirculating separated flow and the freestream flow, and smoothly reattaches to the downstream surface some distance aft of the step. The typical pressure rise on the surface behind the step is shown in Fig. 7.

To represent these observed physical characteristics in the CFD analyses, the simple base separation model shown in Fig. 8 was developed. The separation region is represented as a short solid body extension between the aft body and the sting. The pressure forces on the body are determined from the pressures acting on the actual body geometry forward of the small body extension.

The body extension was represented by a cubic equation that matches the body radius, slope, and second derivative at the end of the body. The body extension continues with a linear variation in the second derivative to zero at the sting intercept station. The sting intercept station, which defines the length of the separation region, is determined by the solution process.

Typical results obtained with this simple separation model are shown in Fig. 9. The effect of the separation model is to essentially move the pressure recovery station aft to the wake reattachment

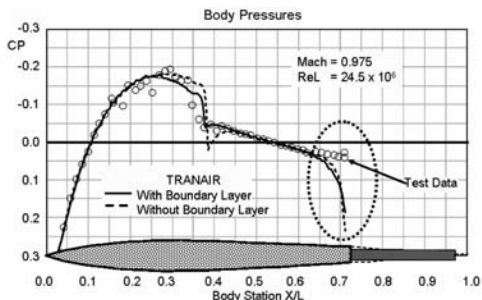


Fig. 4 Initial test vs theory pressure comparisons for the $X/L_{max} = 30\%$ body.

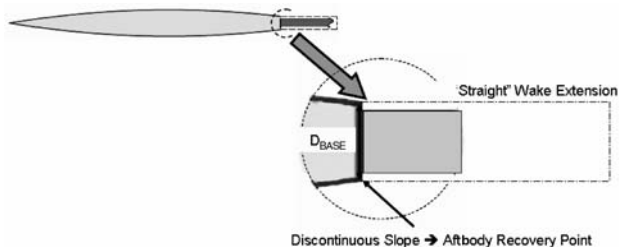


Fig. 5 Typical “straight wake” analysis model.

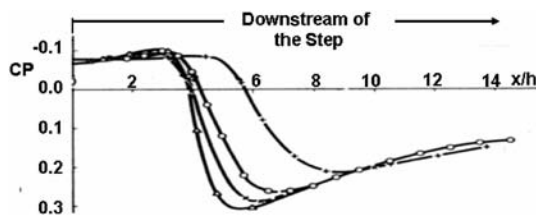


Fig. 7 Characteristics of the pressure distribution downstream of an aft facing step.

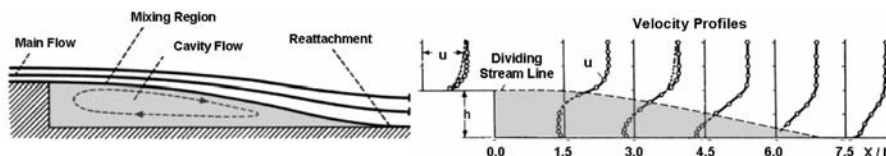


Fig. 6 Separated flow characteristics over a backward-facing step.

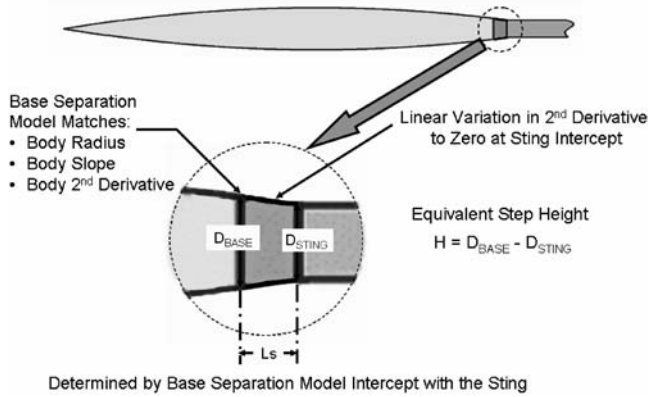


Fig. 8 Base separation model (cubic equation).

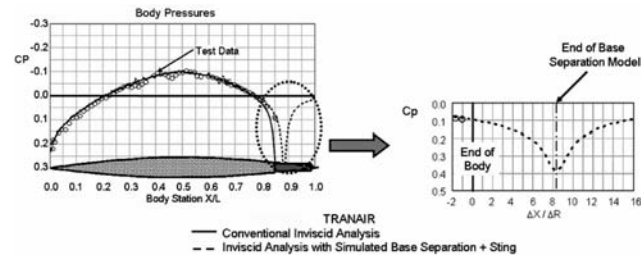


Fig. 9 Effect of the simulated base separation wake on aftbody recovery pressure distribution.

region on the sting. Consequently, the analyses pressures at the aft end of the model now closely match the test data. It will be shown later in this paper that the aft movement of the pressure recovery off the body and onto the sting has a significant effect on the pressure drag of the body at subsonic and near-sonic speeds. The separation model was therefore incorporated in the majority of the subsequent inviscid and viscous studies both with and without the simulated wind-tunnel walls.

Table 3 summarize the study analyses that have been made, the results of which will be discussed in this paper. Inviscid analyses were made with and without the base separation model for all subsonic through low-supersonic Mach numbers, for all of the body geometries. The bodies with base separation extensions were also analyzed at the near-sonic Mach numbers with a coupled boundary layer both in free air and also with the porous wind-tunnel walls represented with a uniform porosity of 0.05. Figure 10 also shows the analysis Mach numbers for which nose shock detachment is estimated to occur for each of the models based on the bodies' nose angles and the corresponding equivalent cone shock detachment conditions.

Body X_{max}/L	Study Mach Number				
	1.025	1.05	1.10	1.15	1.20
30%					
40%		Detached Nose Shock			
50%					
60%					
70%		Attached Nose Shock			

Fig. 10 Nose shock detachment conditions.

$X_{max} / L = 30\%$ Body Analyses Results

The $X_{max} / L = 30\%$ body has a rather large forebody nose angle and mild aftbody slopes. The overall truncated body length for this body is equal to 70.8% of the theoretical body length L . As shown in Fig. 10, this body will have a detached leading shock for all of the analyses' supersonic Mach numbers.

Comparisons of predicted and experimental local Mach number and pressure coefficient C_p distributions, for the $X_{max} / L = 30\%$ body are shown in Fig. 11 for freestream Mach numbers of 0.80, 0.90, 0.95, and 0.975. The theoretical inviscid predictions were obtained both with and without the aftbody wake separation model.

For all of the Mach numbers, the wake separation model has the effect of moving the aft recovery station off the body and aft onto the sting near the wake flow reattachment location on the sting. The theoretical predictions obtained with the base separation model closely match the test data for the freestream Mach numbers of 0.8 and 0.9. For these conditions, the flow is subsonic over the entire body. At a freestream Mach number of 0.95, there exists a region of slightly supersonic embedded flow near the maximum radius station. The experimental pressures show slight oscillations in that region. The overall agreement between the test data and corresponding predictions is still quite good.

At Mach 0.975, a large region of supersonic flow exists on the front portion of the body that is terminated by a strong shock which appears aft of the maximum radius station. The test data indicate that the shock is smoothed out and moved slightly forward relative to the predicted inviscid shock location.

In all the analyses shown in the figure, the base wake separation model closely matches the pressures on the aft end of the model.

Figure 12 shows local flowfield experimental vs theoretical pressure distribution comparisons at radial stations located one to four times the maximum diameter from the body axes. The figure also contains the corresponding experimental and theoretical flowfield constant Mach number contour maps. The theoretical predictions were obtained with and without the base wake simulation model.

The results show that the effect of the aft movement of the pressure recovery effect due to the real flow base separated wake is a relatively

Table 3

Mach number	Analysis models for all bodies					Test data
	Body analysis	Add wake simulation	Add boundary layer	Add wind-tunnel walls		
0.800	X	X	—	—	—	○
0.900	X	X	—	—	—	○
0.925	—	—	—	—	—	○
0.950	X	X	—	—	—	○
0.975	X	X	X	—	△	○
0.990	X	X	—	—	—	—
1.000	—	—	—	—	—	○
1.020	—	—	X	—	△	—
1.025	X	X	X	—	△	○
1.050	X	X	X	—	△	○
1.075	X	X	—	—	—	○
1.100	X	X	X	—	△	○
1.150	X	X	—	—	—	○
1.200	X	X	—	—	—	○

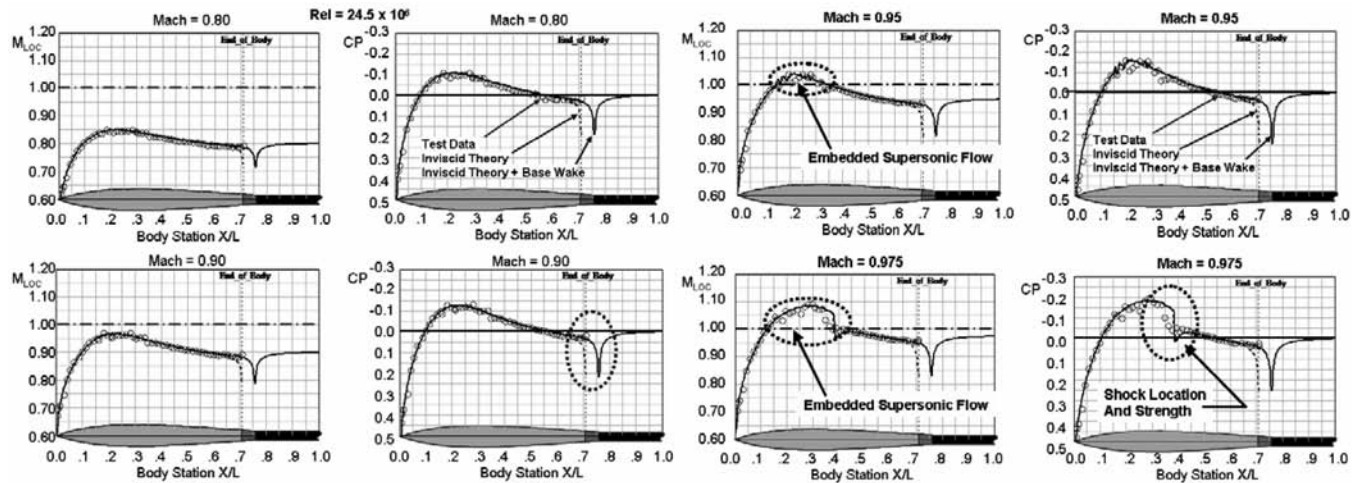


Fig. 11 Test vs theory mach number and CP comparisons for $X_{max} / L = 30\%$ body.

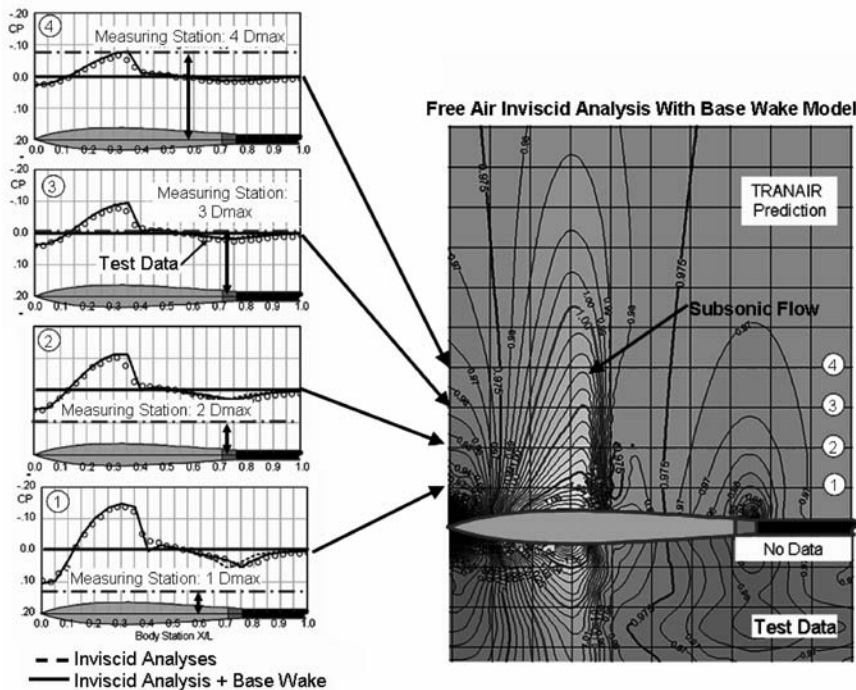


Fig. 12 Local flowfield pressures for $X/C_{max} = 30\%$ body at Mach 0.975 (VFD).

near-field effect that is evident only out to a radial distance of approximately one to two maximum body diameters from the body axes. The agreement between the near-field pressure recovery test data and the CFD predictions tend to further validate the aftbody flow separation wake model developed and used in the current study. The overall theoretical and experimental flowfield Mach contour maps are in very good agreement.

Figure 13 shows the effects of enhancing the analysis model at a freestream Mach number = 0.975. A number of different analyses were made to determine the individual effects of the simulated base wake, the body boundary layer, and the wind-tunnel interference. Additional analyses were made to identify any synergisms between the enhanced modeling elements.

Figure 13a shows the predicted inviscid pressure distributions with and without the simulated base wake. The inviscid analysis indicates a very strong shock that is located slightly aft of the softened shock indicated by the test data. The inviscid solution also indicated a strong pressure recovery that is not evident in the test data.

The addition of the simulated base wake separation model moved the aft recovery region off the body onto the sting and consequently

the predicted recovery pressures on the aft body closely matched the test data.

Figure 13b shows the effect of the body boundary layer without including the base wake. The analysis with the coupled boundary layer softened the predicted shock and moved the shock slightly forward and significantly improved the agreement with the test data in this region on the body. The boundary layer had no effect on the aft recovery pressure distribution.

Figure 13c shows a comparison of an inviscid free-air analysis of the model plus the base wake vs an inviscid analysis of the same geometry but including the wind-tunnel walls in the analyses. As shown in this figure, the primary effect of the wind-tunnel walls was to move the shock forward to the experimental shock location.

Figure 13d shows the combined effects of including the base wake, the body boundary layer, and the wind-tunnel walls on the pressure distribution. The resulting pressure distribution displays the combined effects of improved aft recovery, forward movement, and softening of the midbody shock, and is seen to closely match the experimental data across the entire model. The effects of the

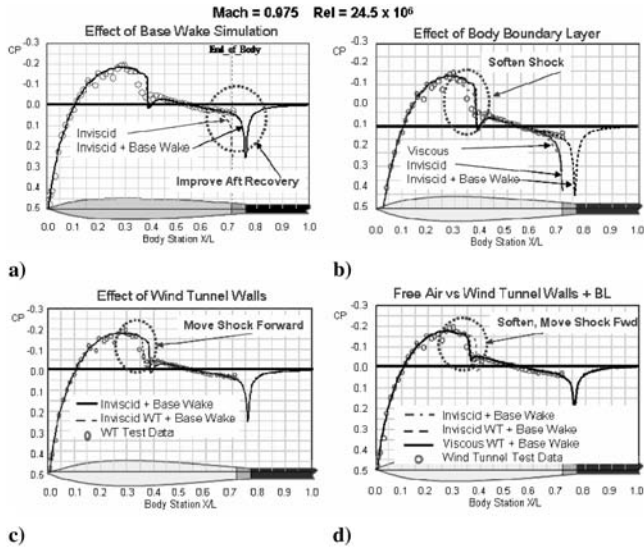


Fig. 13 Effect of enhanced analyses model on CP predictions for X max =30% parabolic body at Mach 0.975.

enhanced analysis model elements appear to be both independent and additive.

Figure 14, which is one form of visual fluid dynamics (VFD), shows a comparison of the Mach number contours in the flowfield computed by the free-air inviscid analysis base separation model, the viscous boundary layer/porous wind-tunnel wall analysis model, and the experimental flowfield data. The effects of the boundary layer plus wind-tunnel walls on the softening and forward movement of the midbody shock is readily apparent. The wind-tunnel walls also limit the radial extent of the large embedded region of supersonic flow near the front part of the body.

Pressure Drag and Total Drag Analyses

Theoretical pressure drags were calculated by integration of the theoretical pressure drags obtained with the various computational models for the X max /L = 30% model.

$$CDP = \int_0^{\psi_m} CP \frac{d\tilde{S}}{d\psi} d\psi \quad (3)$$

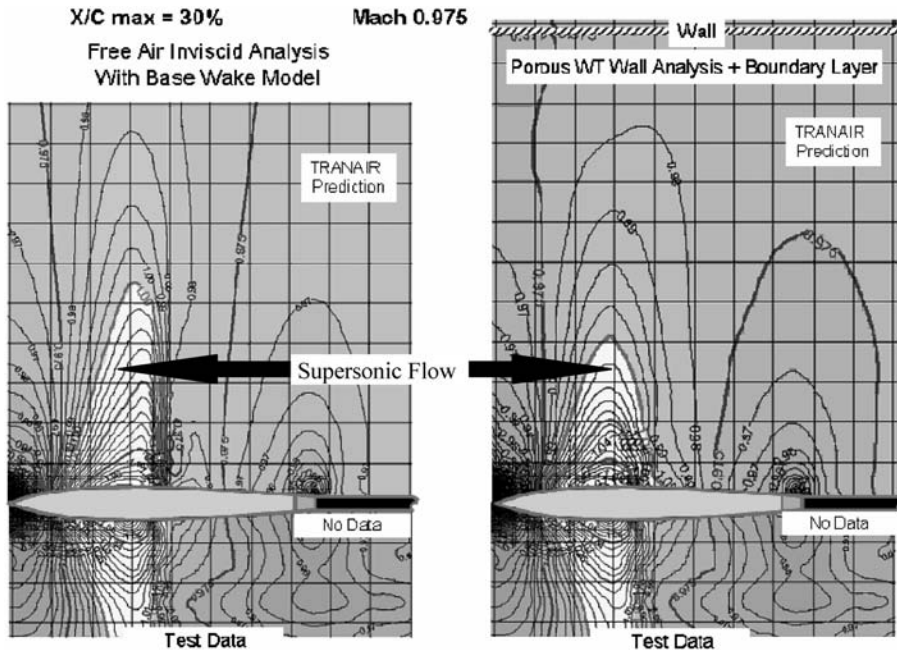


Fig. 14 Effect of wind-tunnel walls on X max =30% parabolic body flowfield, Mach 0.975 (VFD).

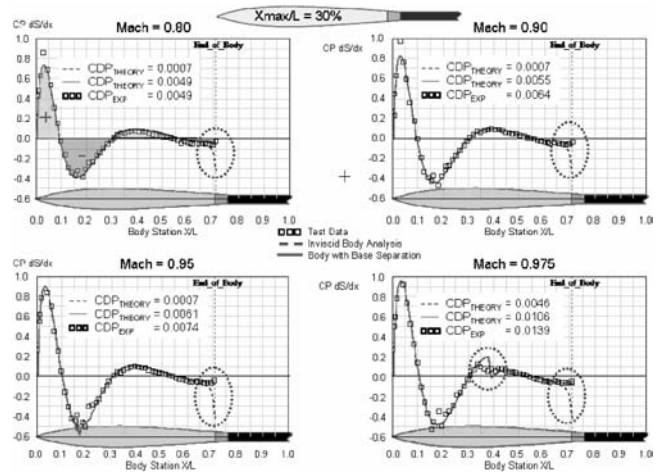


Fig. 15 Sectional pressure drag distributions.

where ψ is the nondimensional length x/L , ψ_m is the value of y at the end of the wind-tunnel truncated body, $\tilde{S}(\psi)$ is the nondimensional area ratio $S(\psi)/S_{max}$, and $CP(d\tilde{S}/d\psi)$ is the sectional pressure drag at the corresponding station ψ .

As previously discussed, the base separation flow model effectively defined a solid body extension to the actual wind-tunnel model to correctly represent the pressure recovery effects on the aft body.

In computing the body pressure drag, the body pressures obtained with the various analytical models are integrated only on the actual wind-tunnel model geometry.

Figure 15 shows the axial distribution of the calculated inviscid sectional pressure drag for the X max /L = 30% body for Mach numbers of 0.8, 0.9, 0.95, and 0.975. The calculation models include the basic wind-tunnel geometry and the analysis model with the simulated base separation region. The experimental axial distributions of the sectional pressure drag, which were determined by integration of the experimental pressure distributions, are also shown. The total integrated pressure drags are also included in the figure.

The data shown in Fig. 15 indicate a large region of drag occurs near the forebody nose followed by a large region of forebody thrust forward of the maximum area.

station there are two smaller regions of drag and thrust. The overall integrated pressure drag is seen to be a relatively small number that corresponds to the net difference between large regions of drag and large regions of thrust (negative drag) on the body. Consequently, seemingly small local changes in pressures (e.g., aftbody recovery pressure distribution) can result in significant effects on the overall net pressure drag.

The predicted pressure drag distribution obtained with the actual wind-tunnel truncated body analyses agrees closely with the experimental data except in the region near the aft end of the model. The incorrectly predicted recovery pressures result in rather significant thrust at the end of the body. The model with the base separation extension essentially eliminates the aftbody thrust. Consequently, the pressure drag predictions without correctly accounting for the flow characteristics at the end of the body grossly underpredict the overall body pressure drag.

The theoretical sectional pressure drag distributions obtained with the base separation extension are in good agreement with the experimental results for the lower Mach numbers. The total integrated pressure drags obtained with the extended base separation analysis model are therefore relatively close to the experimental integrated pressure drags.

At Mach 0.975, the inviscid base extension model pressure drag distribution differs from the experimental results in the midbody region where a strong shock is predicted to occur. As previously discussed, at this Mach number the presence of the wind-tunnel wall also affects the pressure distribution in the region of the midbody shock.

Figure 16 shows the effect of increasing the sophistication of the analytical model to include both viscous and wind-tunnel wall interference effects. The effect of the boundary layer and the effect of the wind-tunnel walls, which affect the pressure distribution in the region of the midbody shock, each increase the predicted pressure drag. The predicted pressure drag including both effects is essentially equal to the experimental pressure drag result.

The theoretical total body drag was calculated as the sum of the flat plate friction drag [13,14] plus the integrated pressure drag. Figure 17 contains a comparison of the both inviscid and viscous total drag predictions with experimental drag obtained by internal balance data corrected by removal of the internal base drag force. The inviscid predictions are those obtained with the base separation extension model. The viscous calculation shown in the figure was obtained by a coupled boundary layer analysis with the wind-tunnel walls simulation.

The agreement between the predictions and the test data is very good for Mach 0.8 and 0.9. As previously shown, the flow was fully subsonic for these conditions. The inviscid predictions slightly

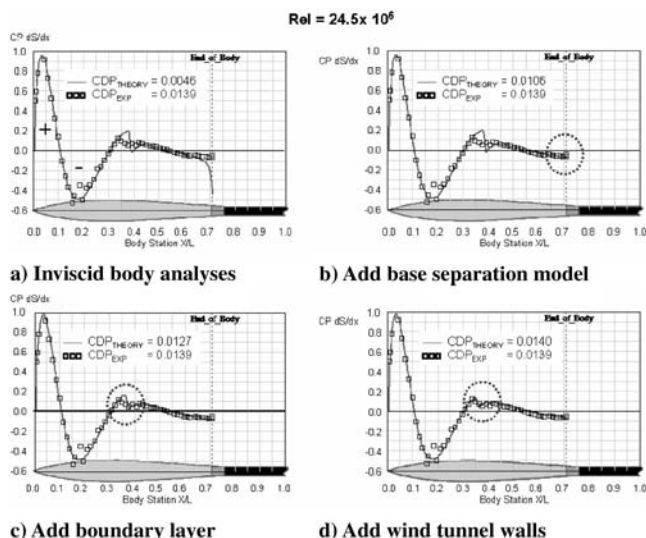


Fig. 16 Effect of analysis model on Mach = 0.975 sectional pressure drag distributions ($X_{max}/L = 30\%$ body).

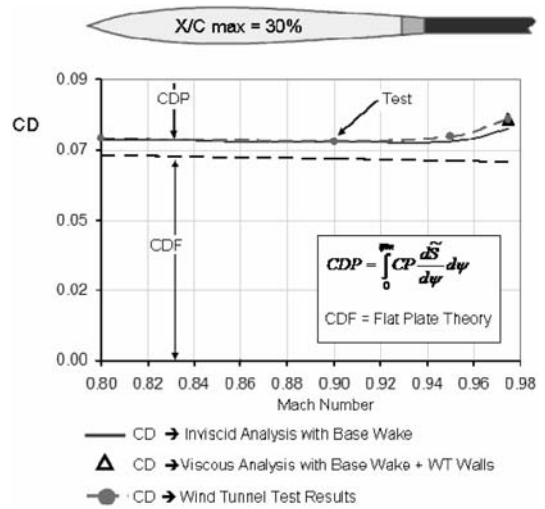


Fig. 17 Predicted and experimental total drag.

underpredict the drag at the transonic and near-sonic conditions of Mach 0.95 and 0.975, respectively.

The viscous prediction at the near-sonic condition agrees closely with the test data.

Figure 18 shows the effect of enhancing the characteristics of the analytical model on the total drag at the near-sonic Mach number of 0.975.

The total experimental or balance drag is shown along with the integrated experimental pressure drag. The difference between the total experimental drag and the integrated pressure drag is considered to be the experimental equivalent of the viscous drag.

The numbers below the bar chart equals the differences between the predicted total drag and the wind-tunnel drag level expressed as a percentage of the total experimental drag.

$$\Delta CD / CDT = \frac{CD - CD_{exp}}{CD_{exp}} \text{ (Percent)} \quad (4)$$

The total drag calculated for the basic wind-tunnel model without the simulated base wake is about 11.4% less than the experimental data. The effect of correctly representing the flow physics at the aft end of the model is seen to be the biggest single factor for improving the theoretical prediction. The viscous drag prediction including the wind-tunnel wall effects is within 1% of the test data.

Low-Supersonic Analyses

As a result of the large nose angle of this body, the nose shock is detached for all of the study's supersonic Mach numbers. The results of low supersonic predictions of the pressure distributions on the

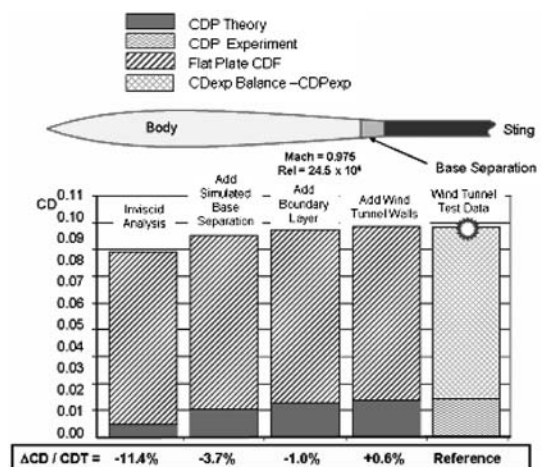


Fig. 18 Total drag for $X_{max}/L = 30\%$ body.

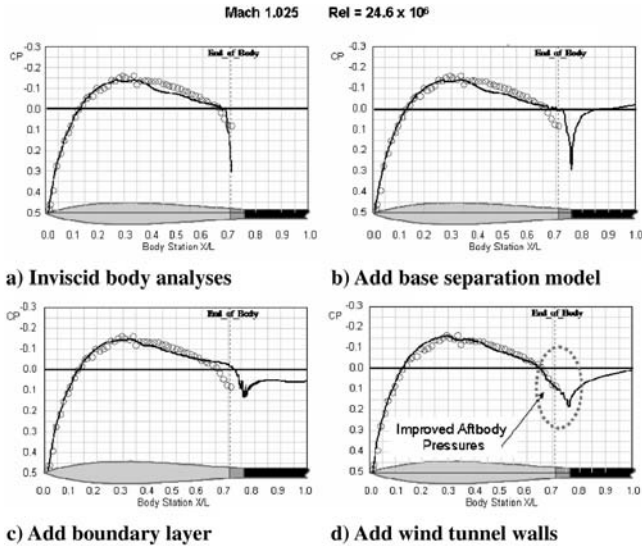


Fig. 19 Mach = 1.025 pressure distributions.

$X_{max} / L = 30\%$ body are shown in Fig. 19 for a Mach number of 1.025.

Figures 19a and 19b compare results obtained from the predictions of the inviscid body pressure distributions obtained with and without the base wake simulation. The experimental pressure data are also shown in the figures. Aft of the body maximum diameter stations, the theoretical predictions differ substantially from the test data.

At the aft end of the body, neither of the inviscid predictions captures the fundamental shape of the recovery pressures. In fact, it would appear that the base wake simulation results in a greater disagreement with the test data.

The addition of the boundary layer as indicated in Fig. 19c resulted in very little improvement in the predicted pressure distribution on the body. The recovery pressure distribution aft of the body is, however, softened by the boundary layer. The viscous predictions obtained with the base wake model together with the wind-tunnel walls interference effects appear to closely match the aft recovery pressure distribution as shown in Fig. 19d. However there are noticeable differences in the predicted and experimental pressure distributions over much of the body.

The results of these analyses show that the boundary layer has a slight overall smoothing effect on the pressure distributions. Contrary to the $M = 0.975$ results, the wind-tunnel wall interference and the base wake both have significant effects on the aftbody recovery pressures at Mach 1.025.

Figure 20 shows free-air inviscid and wind-tunnel viscous predictions of the local flowfield pressure distributions, along with the corresponding experimental measurements, at a number of radial

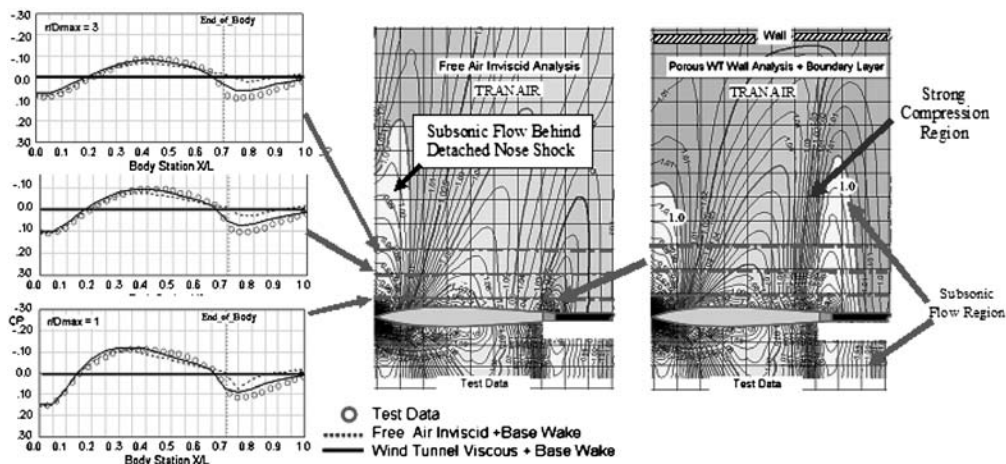


Fig. 20 Comparison of theoretical and experimental flowfield measurements $X_{max} / L = 30\%$, body at Mach 1.025.

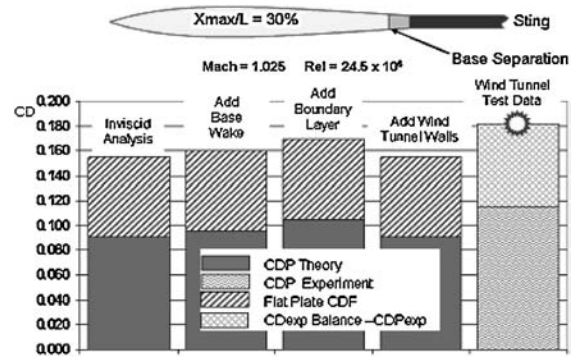


Fig. 21 Comparison of theoretical and experimental drag.

stations from the body for Mach 1.025. The wind-tunnel test data and the viscous predictions indicate a strong recompression in the pressure distributions originating at about 70% of the body length that is not evident in the free-air predictions. This results in an embedded region of subsonic flow which therefore extends radially far from the body. Consequently, the differences between the inviscid free-air predictions and the wind-tunnel data also persist far from the body.

Figure 20 also contains experimental local Mach number contours around the body along with the local Mach contours obtained from the base wake model free-air inviscid predictions, and the viscous porous wall wind-tunnel analyses. A region of embedded subsonic flow behind the detached nose shock is evident in the figures. The free-air inviscid analysis results show a small area on embedded subsonic flow aft of the body in the base wake reattachment region. The predicted effect of the wind-tunnel wall interference is to dramatically increase the size and radial extent of the aft embedded subsonic flow region. The large aft region of subsonic flow is also evident in the test data. The viscous wind-tunnel predictions and the test data clearly show the strong recompression region near the aft end of the body that persists well out into the flowfield.

Figure 21 contains a comparison of the drag at Mach 1.025, calculated by the previously discussed methods, together with the corresponding experimental drag.

All of the analytical models underpredict the pressure drag and, consequently, the total drag at this condition. These results, together with those of Fig. 20, indicate that the model at this test condition experienced significant wind-tunnel wall interference effects which were not adequately predicted by the porous wall viscous analyses. The results also indicate that the experimental porous wall configuration was unable to produce an equivalent free-air environment.

The results of similar low supersonic predictions of the pressure distributions on the $X_{max} / L = 30\%$ body are shown in Fig. 22 for a

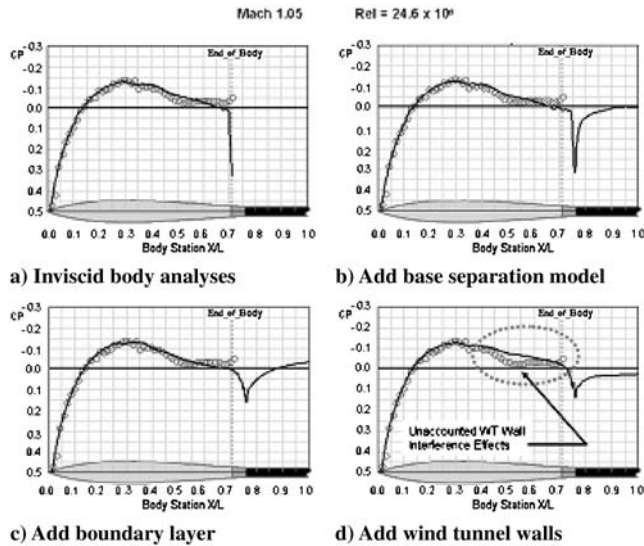


Fig. 22 Pressure Distribution Comparisons for Mach 1.05.

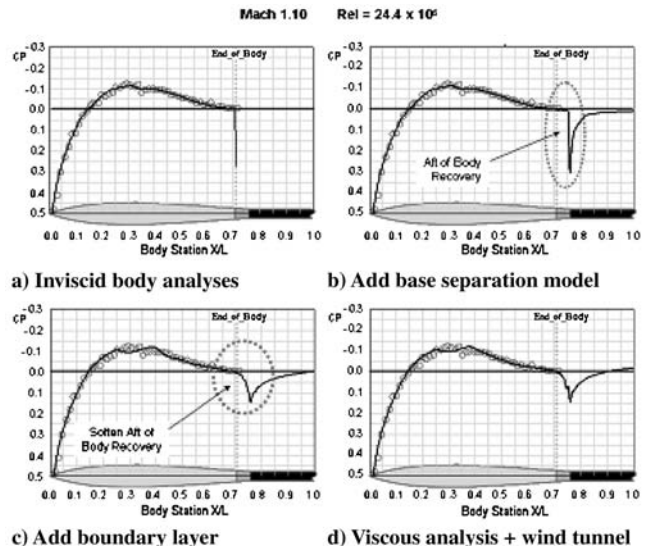


Fig. 24 Pressure distribution comparisons for Mach 1.10.

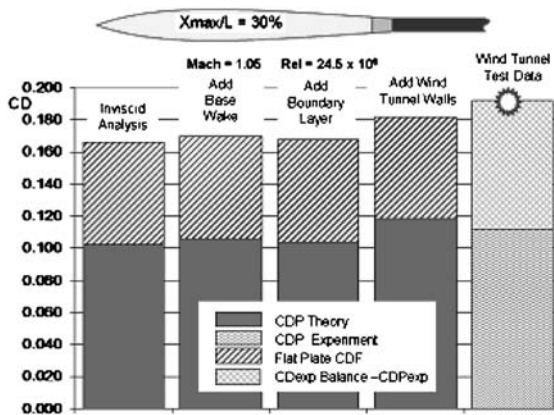


Fig. 23 Theoretical and experimental drag components at Mach 1.05.

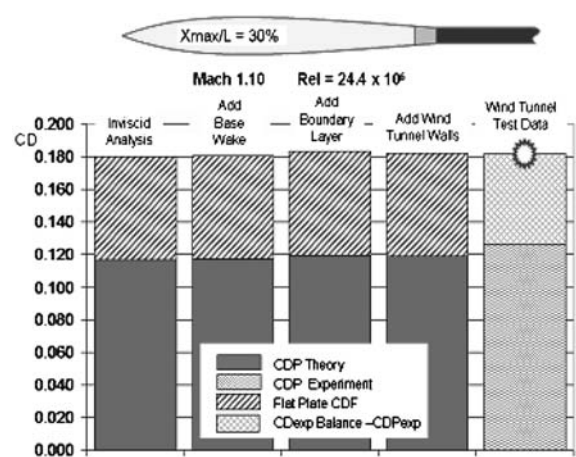


Fig. 25 Mach 1.10 drag components.

Mach number of 1.05. The corresponding theoretical and experimental drag components are shown in Fig. 23.

At this increased low-supersonic Mach number, the experimental pressure results indicate that the wind tunnel at this condition was again unable to produce an equivalent free-air condition. Furthermore, the theoretical analyses did not predict the significant wind-tunnel wall interference effects evident in the data.

Results of the studies at $M = 1.1$ are shown in Figs. 24 and 25. The viscous and inviscid predicted pressure distributions on the body all agree quite closely with the experimental data at this Mach number.

Figure 26 shows a comparison of inviscid free-air and viscous wind-tunnel predictions of the local flowfield at Mach 1.10. The corresponding experimental results are also shown. The entire flow surrounding the body is supersonic except in a small region behind the detached nose shock. The differences between the free-air inviscid pressure distributions and the test data aft of the truncated end of the body show a pressure recompression region apparently due to the wind-tunnel wall effects. The local Mach number contours indicate that neither of the analysis models predict the pressure recompression that is evident in the test data.

Inviscid drag predictions obtained with the simulated base wake are compared with the viscous drag predictions including wind-tunnel wall effects and with the corresponding experimental data in Fig. 27 for subsonic through low-supersonic Mach numbers.

The theoretical predictions agree well with the test data except at the lowest supersonic Mach numbers (Mach 1.025 and 1.05). The difference in the drag predictions is believed to be due to wind-tunnel interference effects that were not adequately captured by the theoretical analysis models.

$X_{max} / L = 40\%$ Body Analyses Results

The $X_{max} / L = 40\%$ body has slightly greater forebody slopes than in the aftbody region. This body will also have detached nose shocks for all of the supersonic analysis Mach numbers (Fig. 10). The truncated wind-tunnel model body length is equal to 78.2% of the theoretical body length L . Figure 28 shows the comparison of the theoretical inviscid predictions of local Mach numbers and surface pressure distributions, with the corresponding test data for the $X_{max} / L = 40\%$ body at Mach numbers of 0.8, 0.9, 0.95, and 0.975. The inviscid predictions were obtained both with and without the simulated base wake model.

The maximum local Mach numbers for this body are lower than those on the $X_{max} / L = 30\%$ body (Fig. 11).

The flow is subcritical (i.e., less than Mach 1) over the entire model until the freestream Mach number exceeds 0.95. The conventional inviscid predictions match the test data except in the region near the aft end of the body. The inviscid model predicts the aft recovery to occur on the body. The analysis model with the base separation wake representation appears to accurately predict the pressure distribution near the aft end of the body.

The overall agreement between the test data and predictions obtained with the base separation model is very good. At Mach 0.975, the theoretical predictions indicate the existence of a very mild shock, just aft of the maximum radius station, which is not readily evident in the test data.

Theoretical near-field pressure distributions and local Mach number contours for the $X_{max} / L = 40\%$ body are compared with

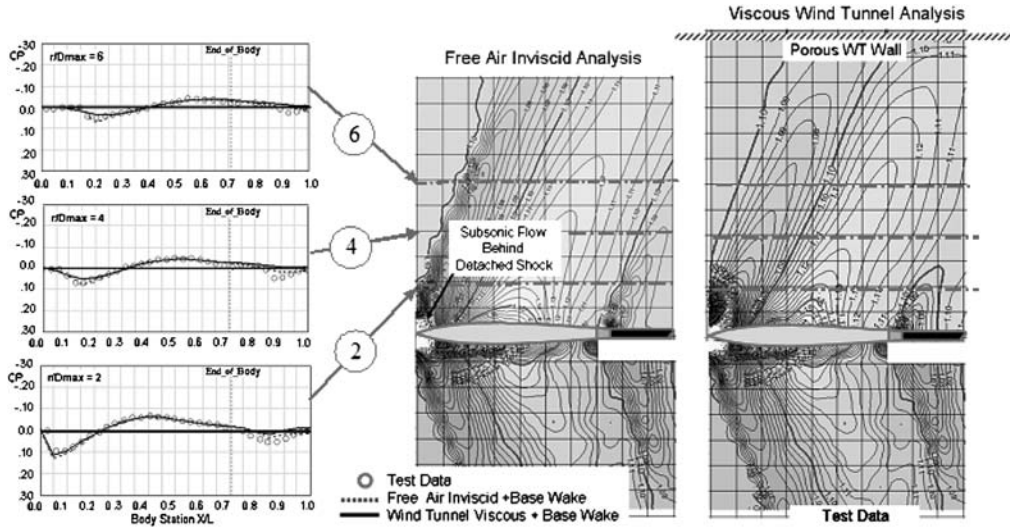


Fig. 26 Free-air and wind-tunnel local flowfield predictions, $X_{max}/L = 30\%$ body at Mach 1.10.

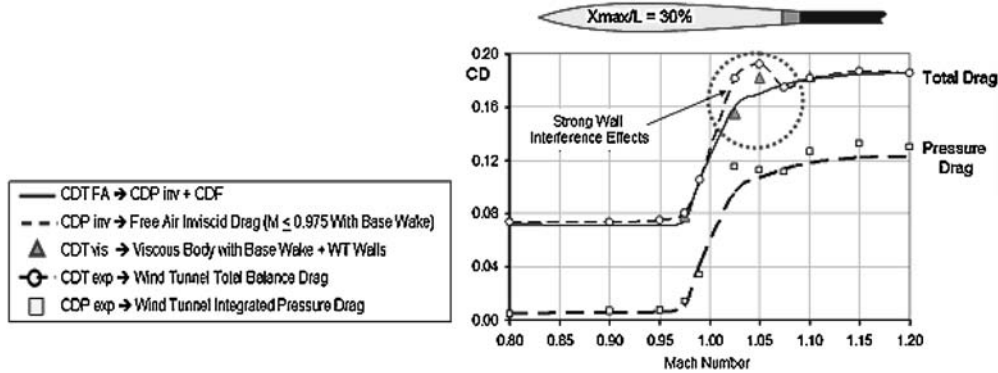


Fig. 27 Subsonic through low supersonic test vs theory drag comparisons.

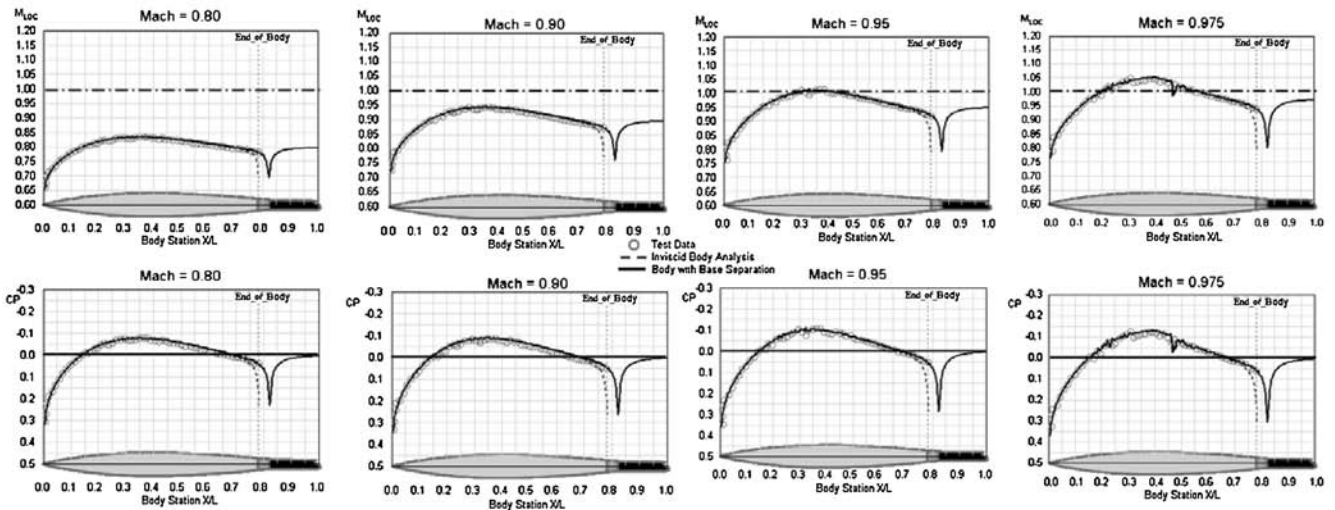


Fig. 28 Test vs theory Mach number and CP comparisons for $X_{max}/L = 40\%$ body.

test data in Fig. 29 for a freestream Mach number of 0.975. The inviscid predictions obtained with the simulated base separation model agree quite well with the experimental measurements. The effects of the base separation wake are seen to influence the local pressure distributions out to approximately a radial distance equal to 1–2 maximum diameters from the body centerline.

The effects of sequentially enhancing the analysis model at Mach 0.975 by including the boundary layer and the wind-tunnel

wall interference effects are shown in Fig. 30. The only apparent effect of the boundary layer was to soften the inviscid shock near the midbody. The predicted wind-tunnel walls interference effects combined with the boundary layer effects, however, appear to fully suppress the shock and thereby closely match the test data which had appeared to show no evidence of a shock.

Sectional pressure drag distributions are shown in Fig. 31 for the $X_{max}/L = 40\%$ body for a range of subsonic Mach numbers. The

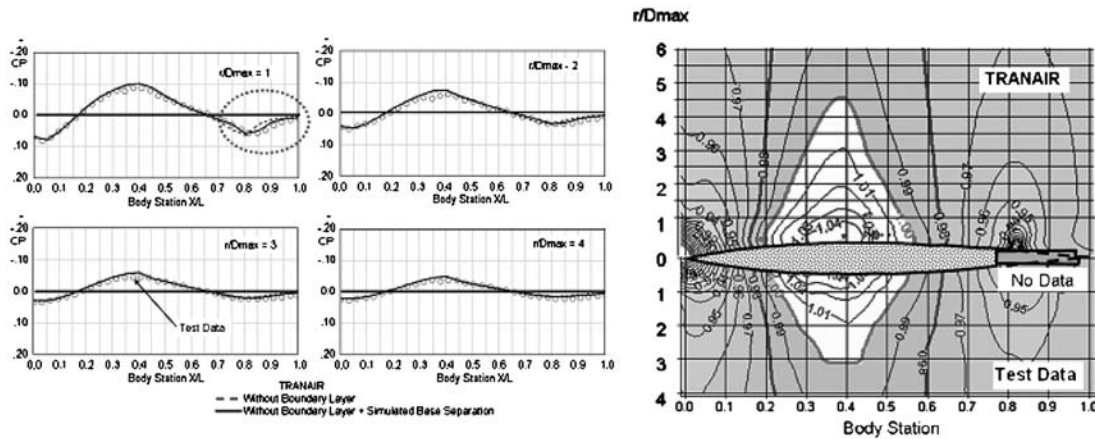


Fig. 29 Local flowfield characteristics for the $X_{max} = 40\%$ parabolic body at Mach 0.975.

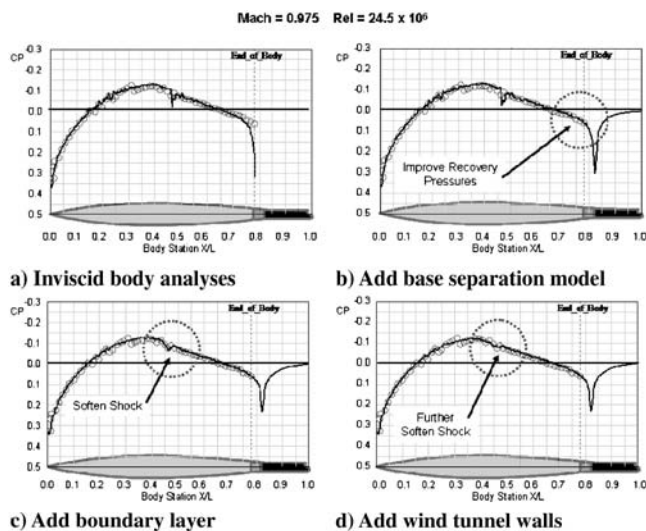


Fig. 30 Effect of enhanced analyses model on CP predictions for $X_{max} = 40\%$ parabolic body at Mach 0.975.

theoretical pressure drag distributions were obtained with the conventional inviscid model and with the simulated base separation model.

The conventional inviscid model results in recovery thrust at the aft end of the model which is not evident in the test data. The overall net pressure drag is once again the difference between large drag regions and large thrust regions on the body. Consequently, the

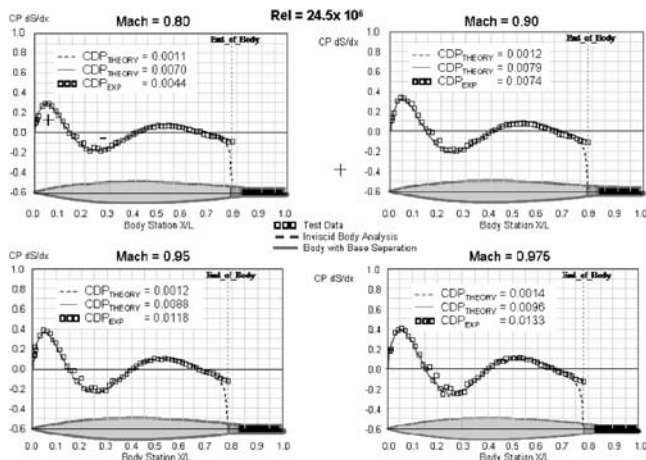


Fig. 31 Sectional pressure drag distributions for $X_{max} / L = 40\%$ parabolic body.

seemingly small change in the drag distributions near the aft end of the body again resulted in a significant change in the net pressure drags.

The effects of enhancing the analytical model on the predicted sectional pressure distributions and the net pressure drag by including the boundary layer and wind-tunnel wall interference effects are shown in Fig. 32 for Mach 0.975. The effects of the boundary layer and the wind-tunnel wall interference on the pressure drag distributions are very subtle and not readily apparent. However the net pressure drag does converge to the experimental result obtained with the experimental pressure distributions as the analytical model is enhanced.

The Mach 0.975 predictions of the total body drag, including skin friction drag plus pressure drag, are shown in Fig. 33 along with wind-tunnel measured balance drag force and the integrated experimental pressure drag.

The skin friction drag is the major contributor to the total body drag. However it can be seen that incorrectly modeling the flow over the aft body, as inherent in the conventional inviscid model, can result in a large error in the overall body drag at near-sonic speeds.

The pressure drag obtained with the base separation wake representations closely matches the experimentally determined pressure drag. However the total drag predictions exceed the total force internal balance drag measurement.

The experimental viscous drag is defined as the difference between the total balance drag minus the pressure drag. Consequently, the experimental viscous drag is about 11% less than predicted by the theory. Because the theoretical predictions

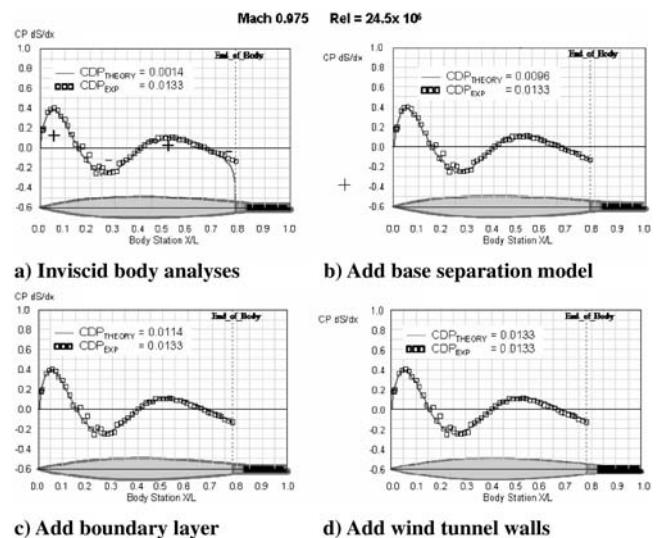


Fig. 32 Viscous and wall interference effects on pressure drag and pressure drag distribution, Mach 0.975.

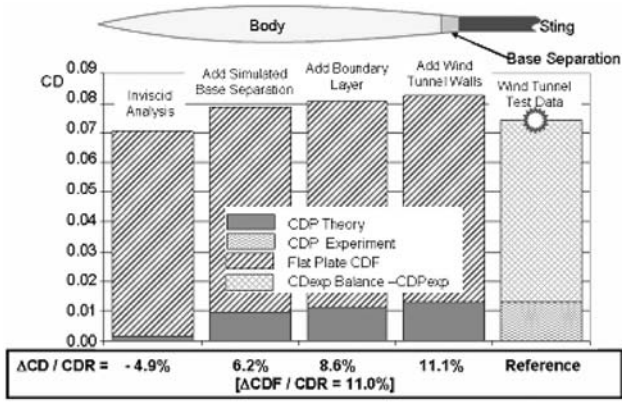


Fig. 33 Predicted and experimental total body drags $X_{max} / L = 40\%$ body, Mach = 0.975.

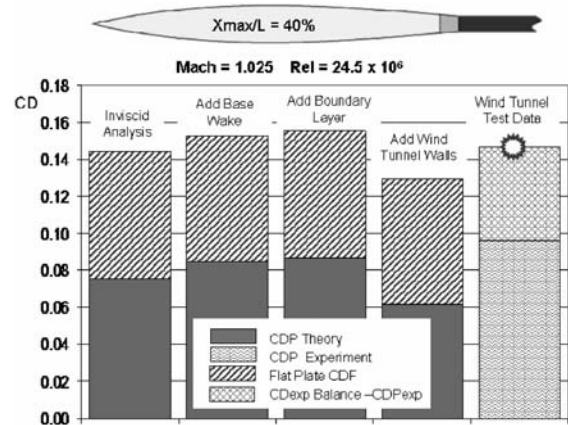


Fig. 35 Total drag for X_{max} / L body at Mach 1.025.

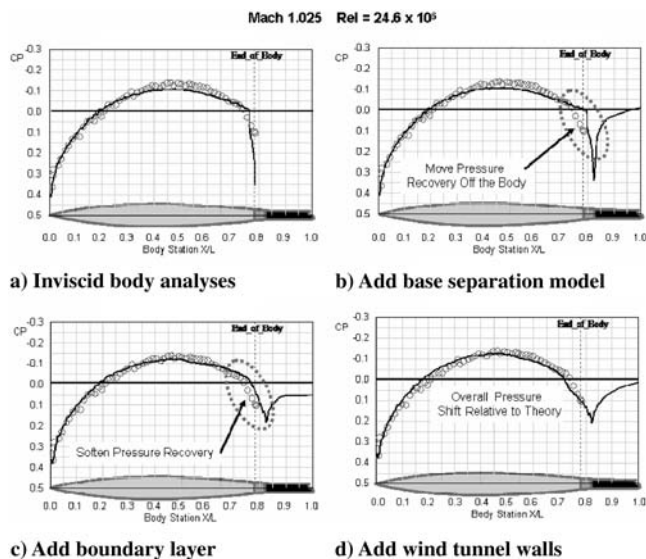


Fig. 34 40% body pressure drag distributions, Mach = 1.025.

were based on fully turbulent flow theory, the “experimental viscous drag” would have to have had a significant amount of laminar flow over the front portion of the model to account for this large drag difference. The models all had a transition trip at about 1 in. from the model [2] which was considered to be effective. Consequently, there must be another source of experimental error to account for the viscous and/or total drag differences.

The theoretical pressure distributions computed with the various analysis models at Mach 1.025 are compared with the corresponding test data in Fig. 34. The results obtained from the viscous analysis on the base separation wake model appear to match the general characteristics of the experimental pressure distribution. However, there appears to be an overall distortion in the pressure distribution due to the wind-tunnel wall interference effects.

The drag predictions obtained with the various analysis models are compared with the test data in Fig. 35. The free-air drag predictions agree better with the test data than the prediction obtained with the porous wind-tunnel wall representation.

Analytical pressure distributions and drag predictions obtained at Mach 1.05 and 1.10 are compared with test data in Figs. 36 and 37, respectively. The experimental data at Mach 1.05 has the similar distorted shape over the last half of the body as did the data for the 30% body (Fig. 22). As previously stated, this is most likely due to wind-tunnel wall interference effects that are not captured in the numerical model and analysis. The inviscid free-air and the viscous wind-tunnel predictions at Mach 1.10 are essentially identical and agree well with the test data.

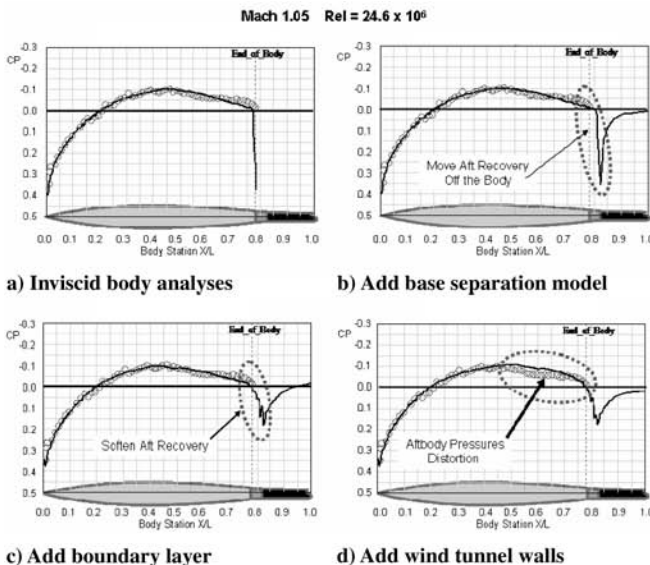
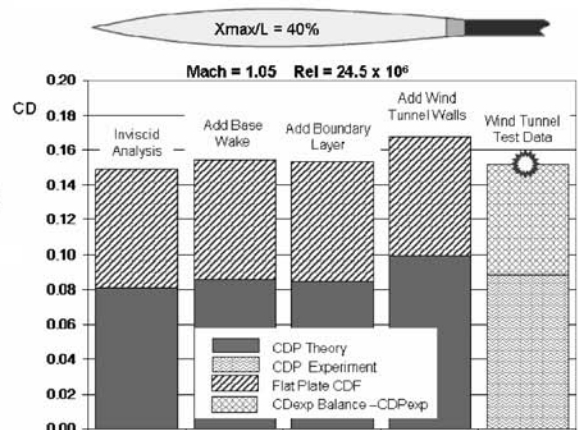


Fig. 36 Surface pressure distributions and drag predictions, Mach = 1.05.



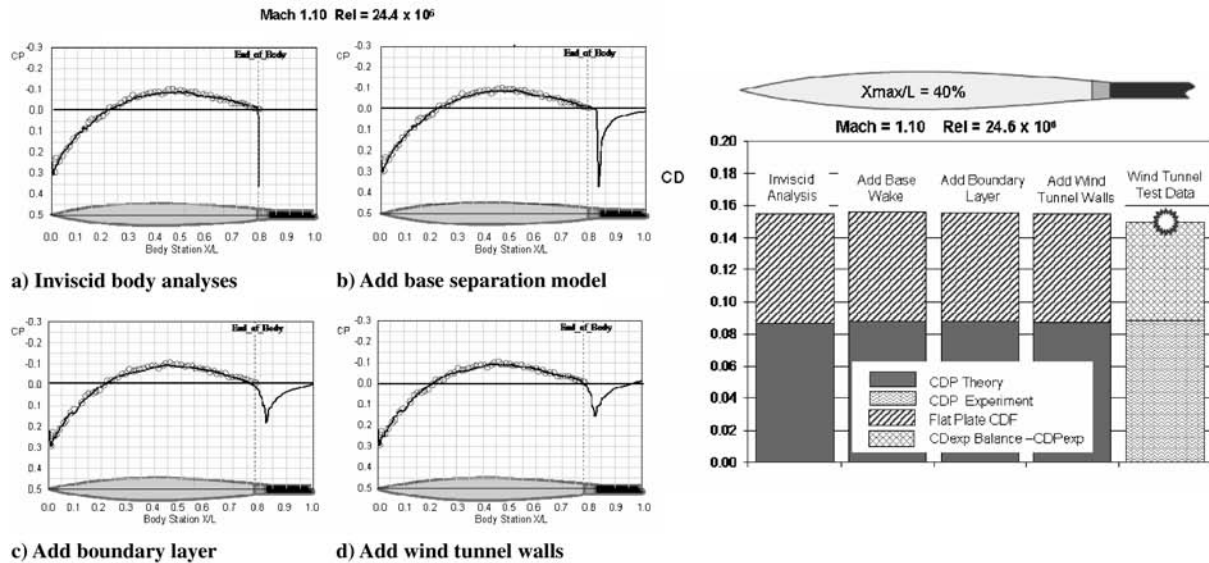


Fig. 37 Surface pressure distributions and drag predictions, Mach = 1.10.

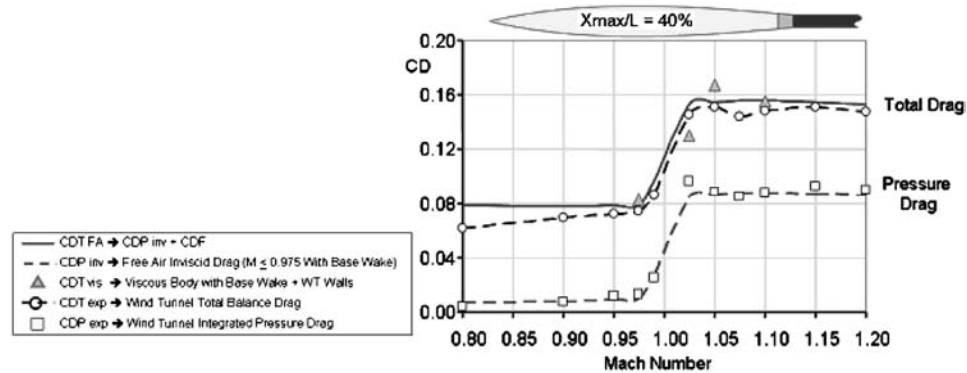


Fig. 38 Total drag buildup.

The theoretical and experimental drag predictions are shown in Fig. 38 for the entire range of subsonic through supersonic Mach number range. The inviscid pressure drag predictions obtained with the base separation model match the test data quite well over the entire subsonic through supersonic Mach range, except for Mach 1.025. The experimentally determined viscous drag at the lowest subsonic Mach number is significantly less than predicted.

X max /L = 50% Body Analyses Results

This section contains the results of the analyses of the X max /L = 50% body. The basic geometry of this body was symmetric about the 50% body station. The overall truncated body length is equal to 85.3% of the theoretical body length L. This body is expected to have a detached nose shock for the analysis supersonic Mach numbers of 1.05 and above.

Figure 39 contains comparisons of theoretical and experimental Mach number and CP distributions on the X max /L = 50% body for a number of subsonic Mach numbers. The theoretical predictions include inviscid body analyses both with and without the simulated base wake. The flow over the body is seen to be subcritical up to a freestream Mach number of 0.975. At that Mach number, there is a small region of supersonic flow near the midbody region. The supersonic flow in this region is just barely supersonic and, consequently, there is no evidence of a recompression shock. The theoretical pressure drag predictions obtained with the base separation model agree well with the test data for the entire range of subsonic freestream Mach numbers.

The predictions obtained without the base wake simulation indicate recompression occurring at the aft end of the body which is not consistent with the test data. The predictions obtained with the simulated base wake closely match the test data. Figure 40 contains comparisons of the corresponding predictions of local flowfield pressure distributions and local Mach number distributions with experimental data. The predictions obtained with the simulated base wake agree closely with the test data throughout the flowfield in which the measurements were made. The effect of the base separation wake is seen to be very localized and vanishes within a radial distance less than two times the body maximum diameter.

The predicted and measured local Mach contours look very similar. The region of embedded sonic flow extends three to four maximum body diameters from the body because the local supersonic Mach numbers in this region are very close to unity.

The sectional pressure drag distributions corresponding to the previously discussed (Fig. 39) experimental and theoretical pressure distributions are shown in Fig. 41. The total integrated pressure drag coefficients are also shown in each chart in the figure. The integrated pressure drags obtained with the simulated base wake are quite close to the test data. The drag values obtained without representing the base wake are significantly less than the test data.

Figures 42 and 43 show the predicted effects of body boundary layer and wind-tunnel wall interference on the surface pressure distribution and corresponding sectional pressure drag distribution for the X max /L = 50% body at the supercritical Mach number of M = 0.975. Because the inviscid predictions obtained with the simulated base wake were in close agreement with the test data, the predicted effects of the boundary layer and wind-tunnel interference

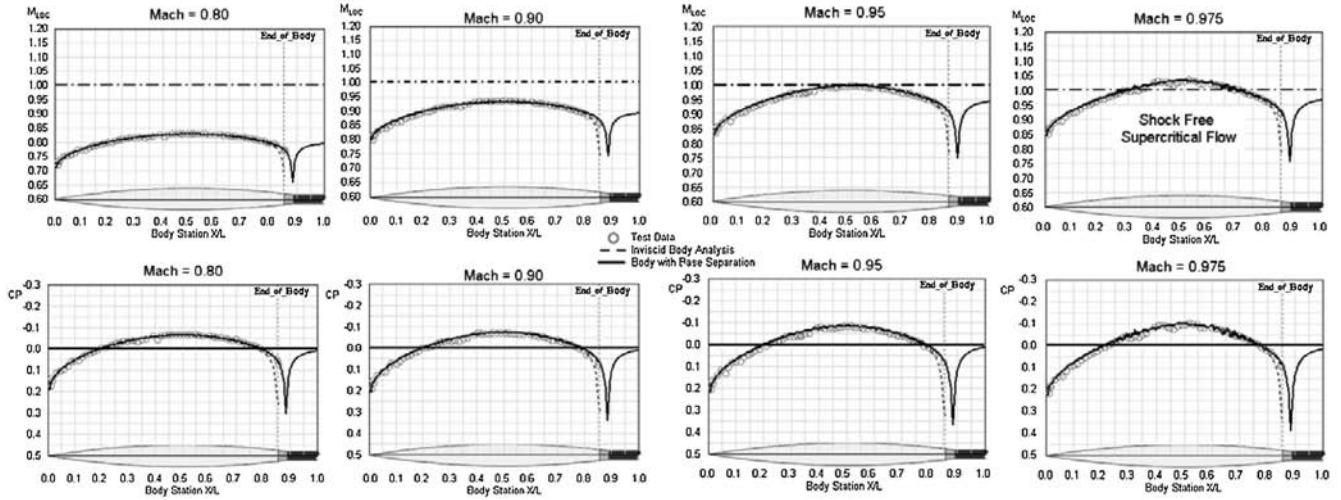


Fig. 39 Mach number and surface pressure distributions for the $X_{max} / L = 50\%$ body.

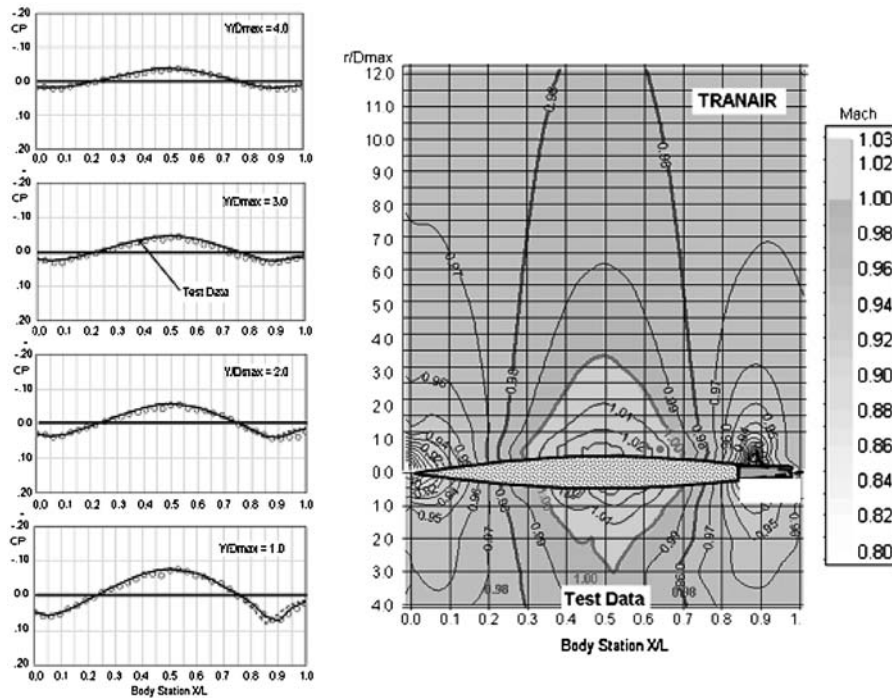


Fig. 40 Local flowfield predictions and measurements, $X_{max} / L = 50\%$ body at Mach = 0.975.

for this body at Mach = 0.975 appear to be negligible even though the predicted drag levels become even closer to the experimental drag level.

The total viscous plus pressure drag components obtained by the various prediction models are shown in Fig. 44 along with the experimental drag data for Mach = 0.975. The theoretical minus experimental drag increments are shown relative to the internal balance force drag measurement below the figure. It is obvious that not representing the base wake region in the analyses can lead to a very large error in the overall drag level. As previously mentioned, the pressure drag obtained with the base wake model and then including the body boundary layer and the wind-tunnel wall effects all match the experimental pressure drag. However the experimental “viscous drag” is once again seen to be less than the fully turbulent viscous drag level.

The results of the CFD analyses of the $X_{max} / L = 50\%$ body at the low supersonic Mach number of $M = 1.025$ are shown in Figs. 45 and 46. The effect of enhancing the CFD model on the body pressure distribution is shown in Fig. 45. Initially it would appear that the predicted pressure distribution obtained without the simulated

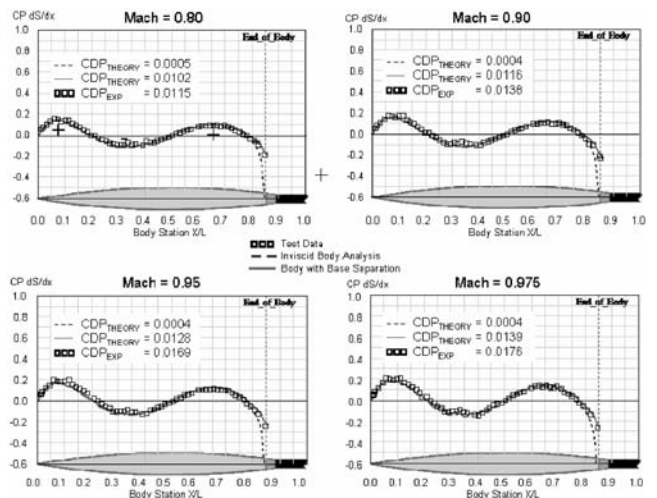


Fig. 41 $X_{max} / L = 50\%$ body subsonic pressure drag distributions.

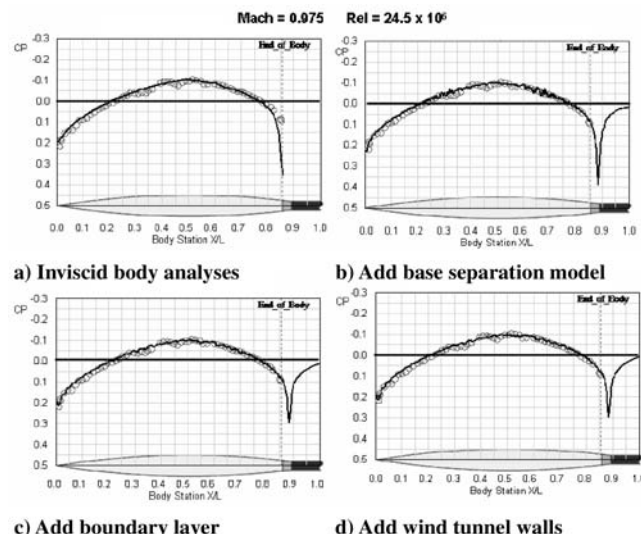


Fig. 42 Predicted effects of boundary layer and wind-tunnel interference on body CP distribution.

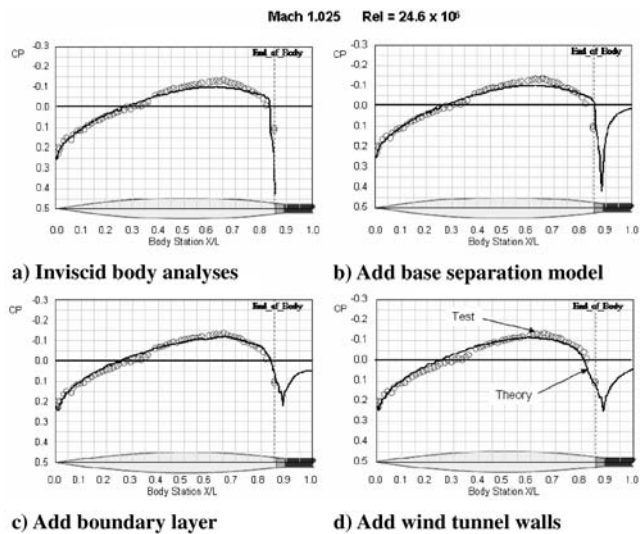


Fig. 45 Predicted body CP distribution for Mach = 1.025.

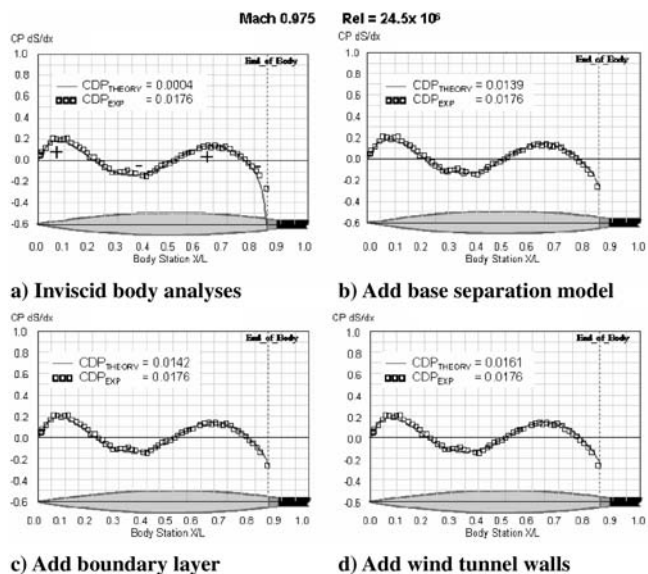


Fig. 43 Effect of boundary layer and wind-tunnel interference on pressure drag.

base wake is slightly better near the aft end of the model than the results obtained including the base wake. However the pressure distribution obtained with the base wake model plus boundary layer is in better agreement with the test data than the inviscid predictions without the base wake. The results obtained with the wind-tunnel wall effects appear to indicate a slight forward movement of the pressure distribution over much of the body and consequently shows less agreement with the test data. The experimental pressure distribution shows a more negative peak than the theoretical predictions. This indicates that the experimental wind-tunnel wall interference effects are more significant than the theoretical predictions.

Figure 46 shows the total drag predictions corresponding to the pressure distributions of Fig. 45. The drag predictions obtained using the base wake model with and without the boundary layer are close to the experimental result. It can be seen that the prediction obtained with the wind-tunnel wall effect resulted in a drag significantly lower than the test data.

Figure 47 shows the effect of freestream Mach number on the flowfield Mach number distribution for the $X_{max}/L = 50\%$ body. For Mach numbers up to 0.95, the flow over the body is subcritical because the flow is entirely subsonic over the body. At Mach 0.975, the flow becomes supercritical because there is an embedded region of supersonic flow in the middle region of the body. At Mach 1.0 the region of supersonic flow extends radially far out into the flowfield. At a low supersonic Mach number of 1.025, the flow over the body is

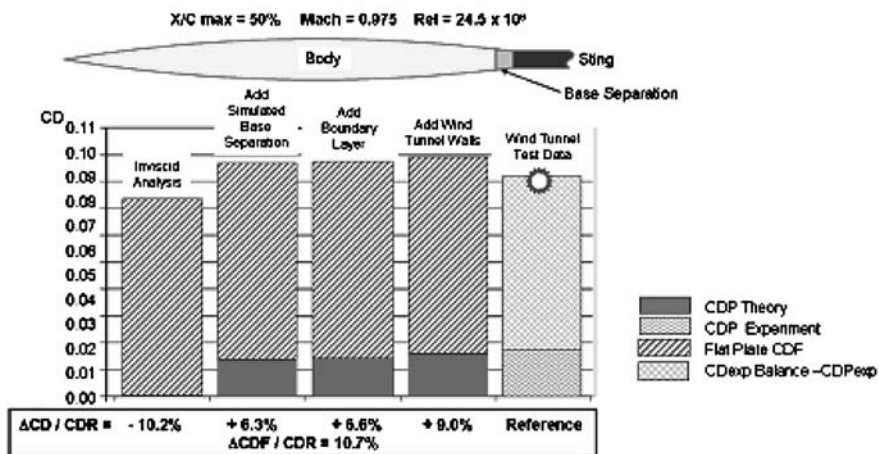


Fig. 44 Total Drag Components at Mach 0.975.

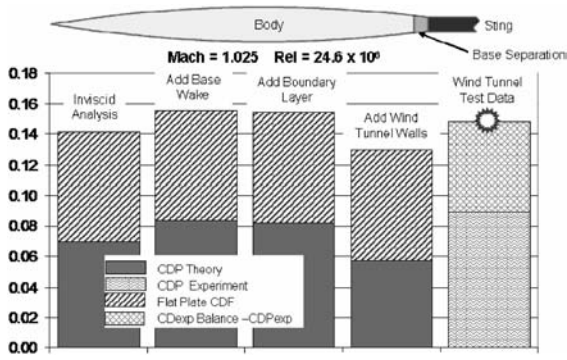


Fig. 46 Total drag components at Mach 1.025.

supersonic except in the compression region near the body nose and in the recompression region just aft of the body.

Figure 48 shows the effect of body fineness ratio (L/D_{max}) on the experimentally obtained local flow characteristics for a family of $X_{max}/L = 50\%$ bodies [1] at a supercritical Mach number of 0.975. The radial extent of the supercritical region is seen to expand rapidly as the maximum diameter increases for a given body length. The magnitudes of the local Mach numbers within the supersonic flow region also increase with decreasing fineness ratio. The parabolic bodies of revolution with various lengthwise locations of maximum radius discussed in this paper all had the intermediate length to maximum diameter ratio of 12.

Results of theoretical analyses of the $X_{max}/L = 50\%$ body at the low supersonic Mach number of 1.05 are shown in Figs. 49 and 50. The theoretical inviscid pressure distribution on the body appears to be on average close to the test data. However a closer examination of the test data shows an irregular variation in the shape of the pressure distribution over the back half of the body. The viscous analysis with the base wake resulted in a more realistic pressure recovery aft of the body. The analysis with the porous wind-tunnel walls included in the analyses was unable match the rather irregular shape of the pressure distribution which is believed to be due to wind-tunnel interference effects.

The inviscid analysis drag prediction is slightly less than the test data. The drag predictions obtained from the inviscid and viscous

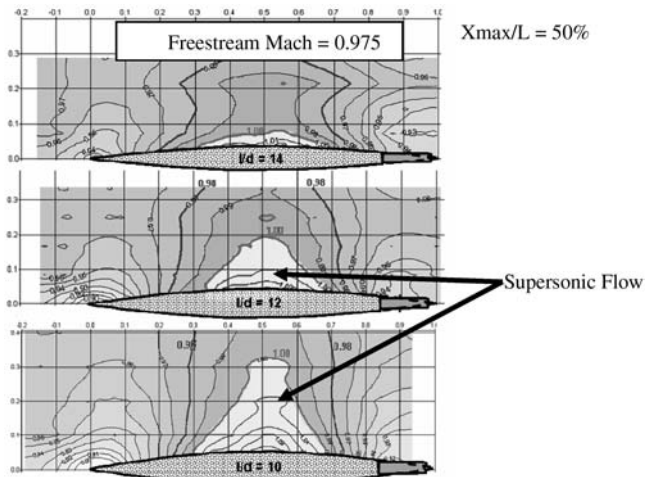


Fig. 48 Effect of body fineness ratio on local Mach number distribution.

analyses plus base wake, and the viscous analysis with base wake and wind-tunnel walls all slightly overpredicted the drag relative to the test data.

The results of the analyses of the $X_{max}/L = 50\%$ body at Mach = 1.10 are shown in Figs. 51 and 52. At this Mach number, the flow over the entire body is supersonic. The inviscid pressure distribution and theoretical drag match the test data quite well. Including the boundary layer, the base wake and wind-tunnel walls in the analyses have essentially no effect on the body pressure distribution or on the total drag. The predicted shape of the recovery pressure distribution behind the body obtained from the viscous analysis with the base wake appears to be more realistic than that of the inviscid analysis.

The results of the analyses of the integrated pressure drags and the total drags for the $X_{max}/L = 50\%$ body are shown in Fig. 53 with the corresponding experimental drags. The predicted pressure drags obtained with the inviscid analyses including the base wake match the experimental drags quite well. The theoretical total drag predictions obtained with the inviscid base wake model plus flat plate

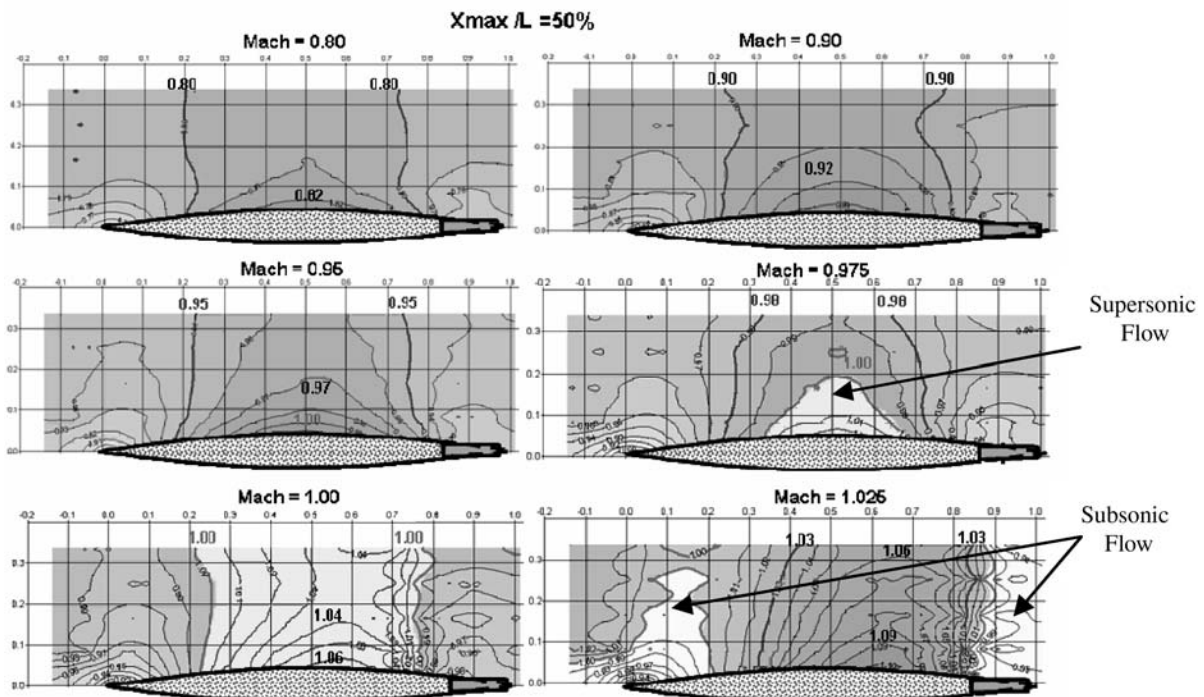


Fig. 47 Effect of Mach number on local flowfield Mach number distribution.

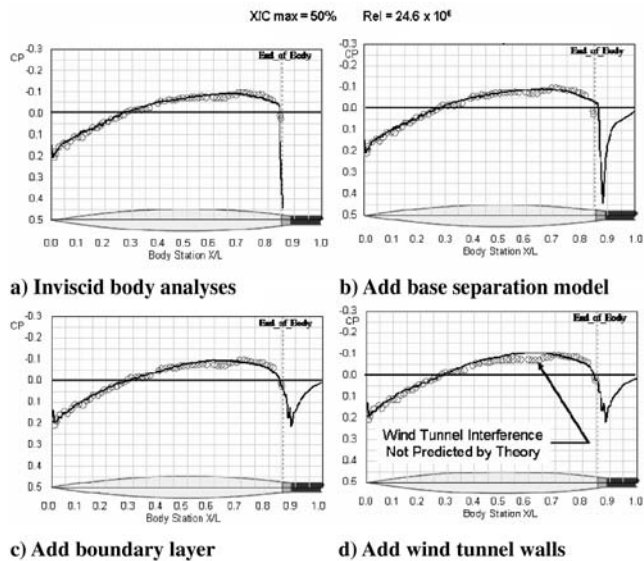


Fig. 49 Effect of analytical model on body pressure distributions, $X_{max}/L = 50\%$ Mach = 1.05.

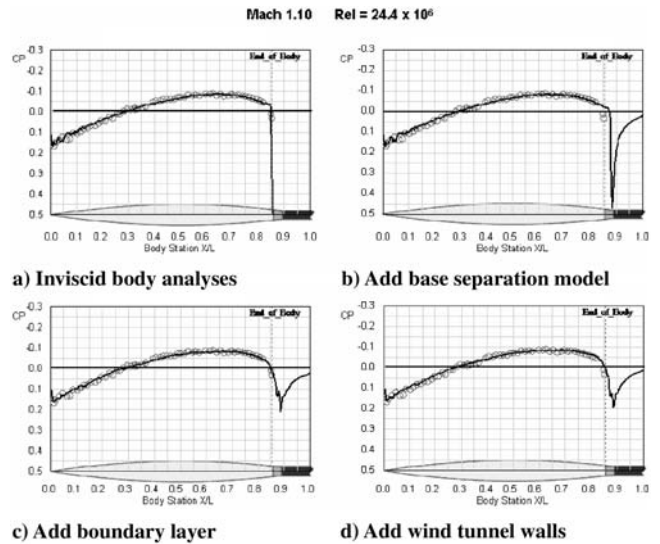


Fig. 51 Effect of computational model enhancement on predicted surface distribution at Mach 1.10.

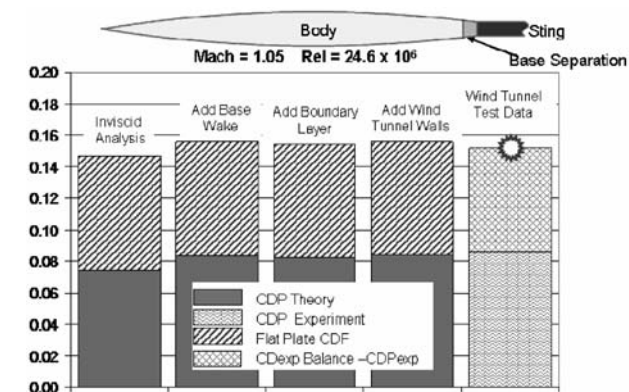


Fig. 50 Drag predictions for $X_{max}/L = 50\%$ body at Mach = 1.05.

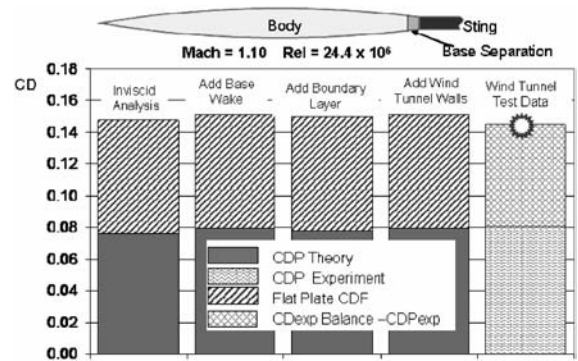


Fig. 52 Drag predictions for $X_{max}/L = 50\%$ body at Mach = 1.10.

skin friction slightly exceed the experimental total drag values. These results lead to the conclusion that the experimental viscous drag is less than fully turbulent flat plat skin friction drag. The agreement between the inviscid plus base wake pressure drag predictions at the low supersonic Mach numbers is quite good even though the corresponding theoretical body pressure distributions differ from the irregular shape of the experimental pressure distributions over the middle part of the body. Because of the low body slopes in this region, which is near the maximum area station, the pressure drag is not very sensitive to the differences in the pressure distributions. It is also seen that the viscous predictions with the wind-tunnel walls did not capture the wind-tunnel wall effects and significantly underpredicted the drag at the low supersonic Mach numbers.

$X_{max}/L = 60\%$ Body Analyses Results

The $X_{max}/L = 60\%$ body is characterized by moderate slopes over the front part of the body and rather large slopes over the aft part of the body. The supersonic nose is estimated to be detached at Mach 1.1 and above. The overall truncated body length is equal to 89.3% of the theoretical body length L . Theoretical and experimental Mach number distributions, pressure distributions, and pressure drag distributions on the body are shown in Fig. 54 for a number of subsonic freestream Mach numbers. The theoretical predictions shown in the figure include inviscid calculations obtained with and without the simulated base wake.

Similar to the results obtained on the other previously discussed bodies, the inviscid “straight wake” calculations result in a strong pressure recovery on the aft body that essentially cancels the pressure drag. The analysis model with the simulated base wake results in a

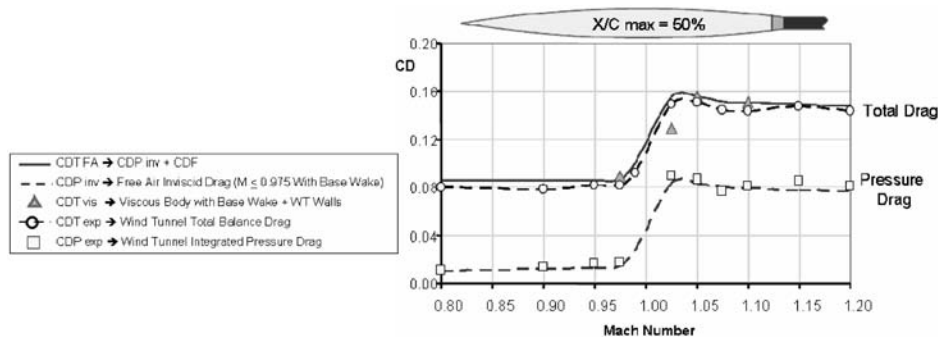


Fig. 53 Comparison of theoretical and experimental drag for the $X_{max}/L = 50\%$ body.

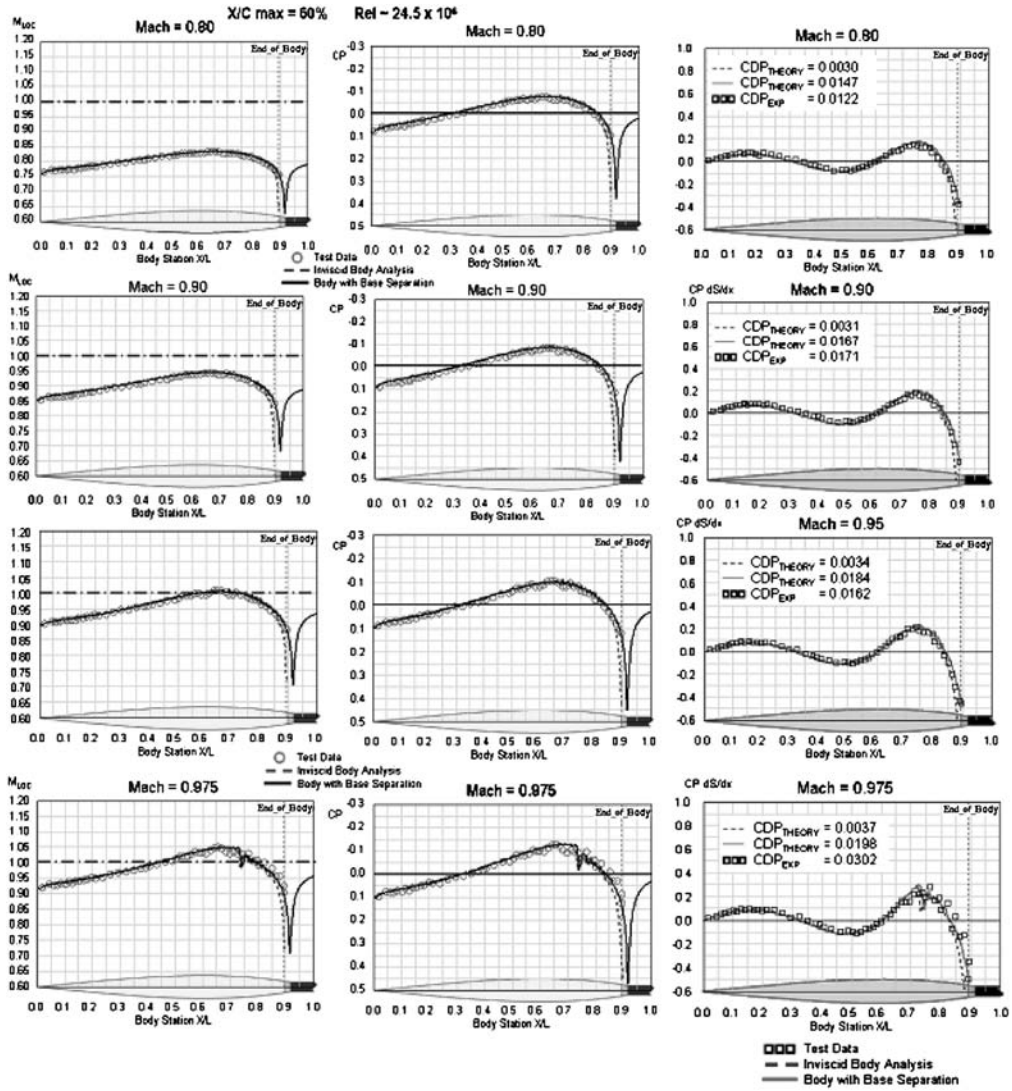


Fig. 54 Subsonic body pressure and pressure drag distributions for the $X_{max}/L = 60\%$ body at subsonic speeds.

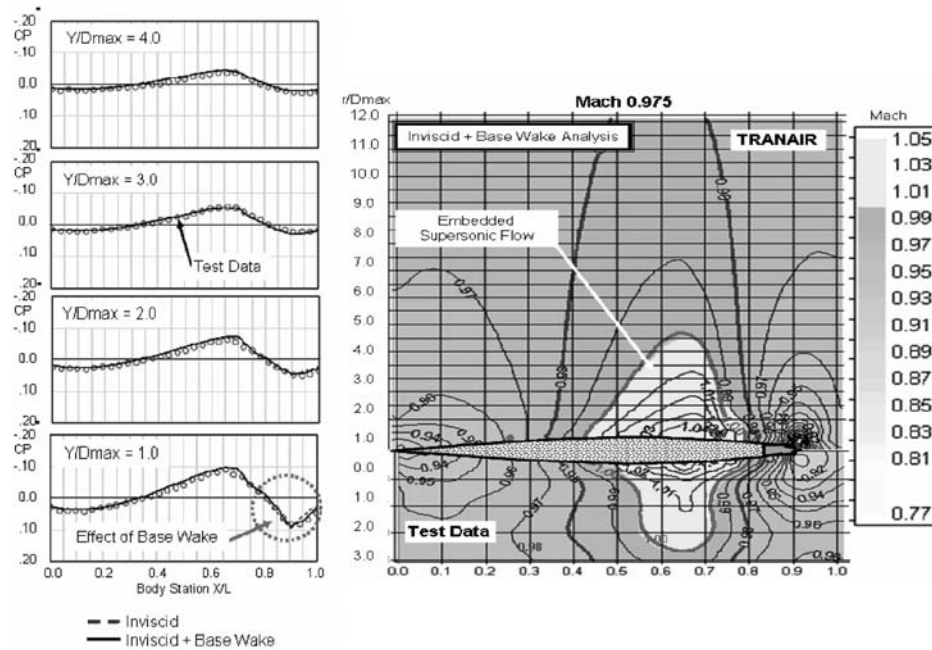


Fig. 55 Near-field pressure and pressure drag distributions for the $X_{max}/L = 60\%$ body.

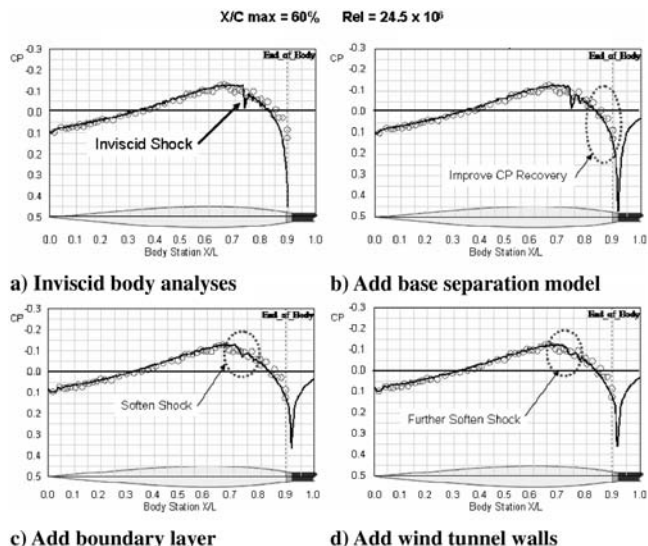


Fig. 56 Effect of enhanced analytical models on predicted pressures for the $X_{max}/L = 60\%$ body.

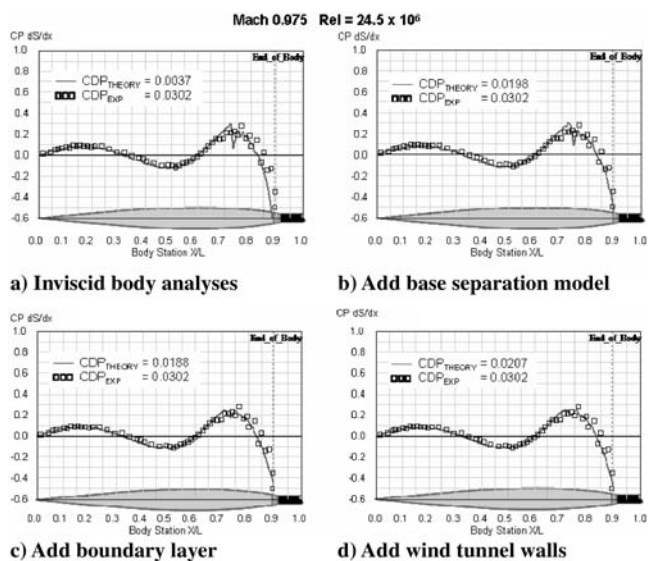


Fig. 57 Effect of enhanced analytical models on predicted pressure drag for the $X_{max}/L = 60\%$ body.

better match to the test data in the aftbody region because with this model the pressure recovery occurs aft of the body near the body wake/sting attachment location. For Mach numbers up to and including $Mach = 0.95$, the flow over the body is fully subsonic and the theoretical predictions agree well with the test data. At $Mach 0.975$ the flow over the body is supercritical with a region of embedded mild supersonic flow. The theoretical inviscid predictions indicate a mild recompression shock, at approximately 75% of the overall theoretical length, which is not evident in the test data.

Figure 55 contains comparisons of theoretical and experimental near-field pressure measurements and local Mach number distributions at $Mach 0.975$. The theoretical predictions include results of the inviscid predictions with and without the simulated base wake. The theoretical predictions agree very well with the test data. There is no evidence of a shock in the near-field experimental data or theoretical predictions. The effect of including the base wake simulation, which was important for the pressure drag predictions, is seen to be very localized in the region of the body aft end and vanishes within a radial distance equal to $2 \times D_{max}$.

The results of the additional CFD predictions of the body pressure distributions at $Mach 0.975$ obtained by including the body boundary layer and wind-tunnel wall effects are shown in Fig. 56 along with the previously discussed inviscid results.

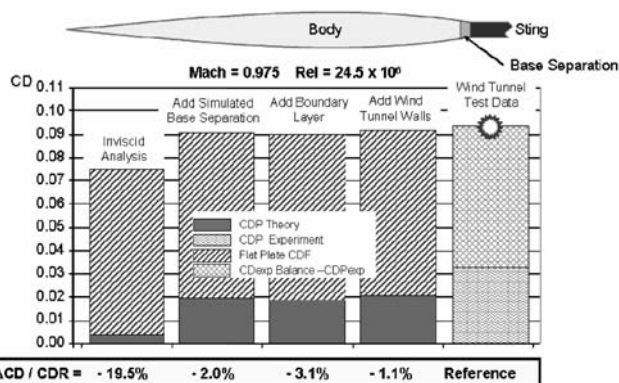


Fig. 58 Drag prediction comparisons for the $X_{max}/L = 60\%$ body.

The primary effect of including the boundary layer is seen to be a softening of the recovery shock, thereby matching the characteristics of the test results. The effects of including the porous wind-tunnel walls are apparently rather insignificant and appear to slightly further soften the body shock.

The corresponding comparisons of the experimental and the theoretical pressure drag distributions are shown in Fig. 57. The effect of the boundary layer in smoothing the recovery shock is also evident in the pressure drag distributions. The theoretical drag predictions obtained by the various analyses methods are all less than the value calculated from the experimental pressure distribution which is characterized by substantial scatter-type variations near the aft end. The scatter in the experimental pressure drag distribution, which is directly related to scatter in the experimental pressure distribution, more than likely has an effect on the calculated experimental pressure drag. The net pressure drag is the difference between a large drag force and a nearly equal thrust force. Consequently, small differences in the pressures in a local region can have a large effect on the net drag.

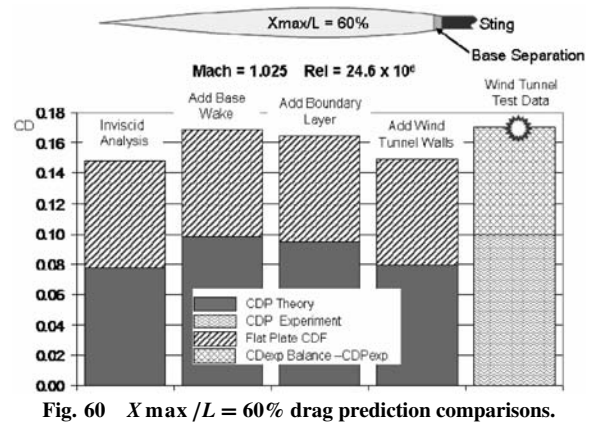
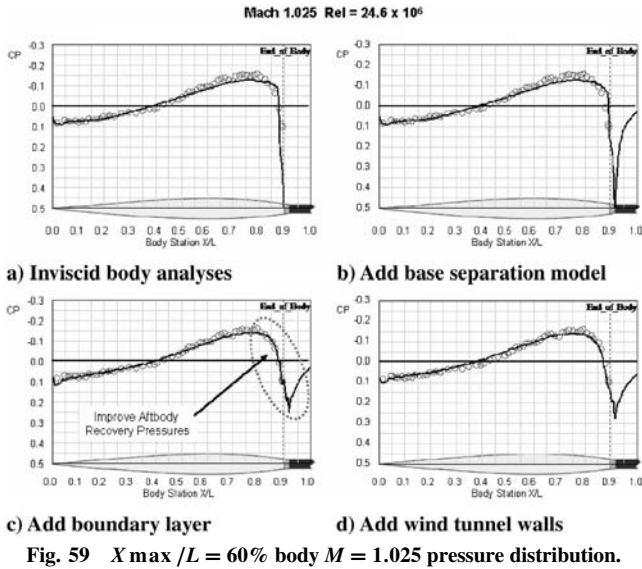
Figure 58 contains the component drag predictions obtained by the various analysis models along with the corresponding experimentally determined values. Including the simulated base separation wake is seen to be very important for an accurate drag prediction on the body at this near-sonic Mach number. The effects of including the body boundary layer and the wind-tunnel walls in the analysis are quite insignificant for the drag prediction for this case.

The results of the $Mach 1.025$ surface pressure predictions and drag predictions are shown in Figs. 59 and 60, respectively. The base wake simulation improves the body aft pressure recovery as well as the pressure drag prediction. The body boundary layer effects are negligible at this Mach number. The effect of simulating the wind-tunnel walls appears to have a slightly beneficial effect in improving the body pressure distribution comparison with the test data but has an adverse effect on the pressure drag prediction. This is another example of the sensitivity of pressure drag determination from surface pressure integration to very slight variations in the characteristics of the pressure distribution.

The results of the analyses and test vs theory comparisons at Mach numbers of 1.05 and 1.10 are shown in Figs. 61 and 62, respectively. The effects of the base separation wake, the boundary layer, and wind-tunnel wall interference all appear to be negligible at these Mach numbers for the $X_{max}/L = 60\%$ body geometry.

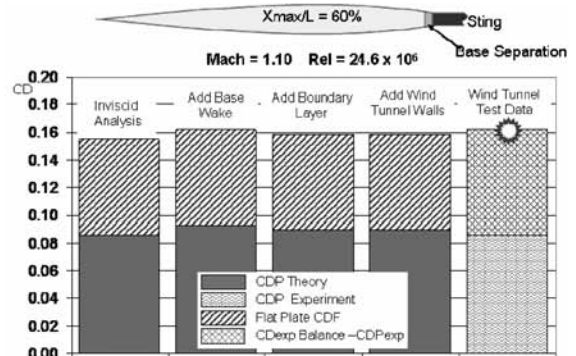
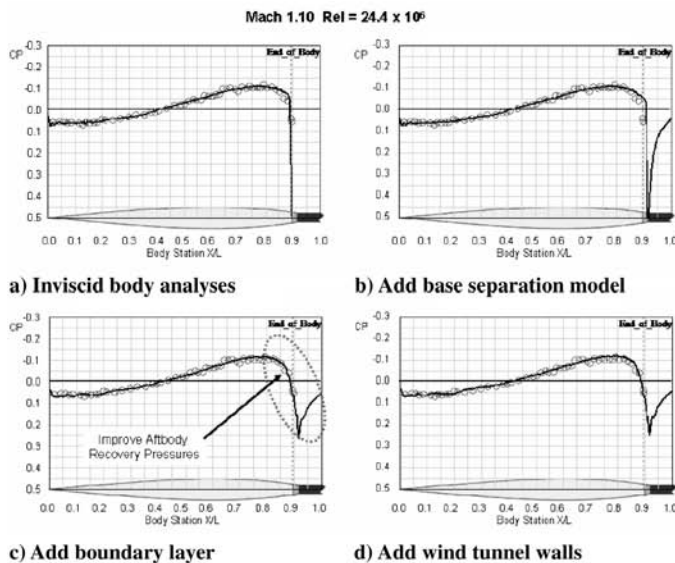
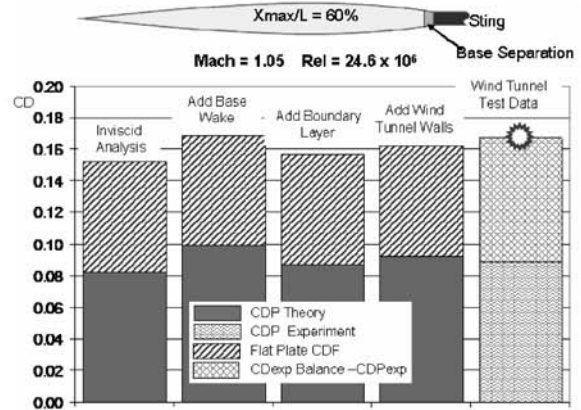
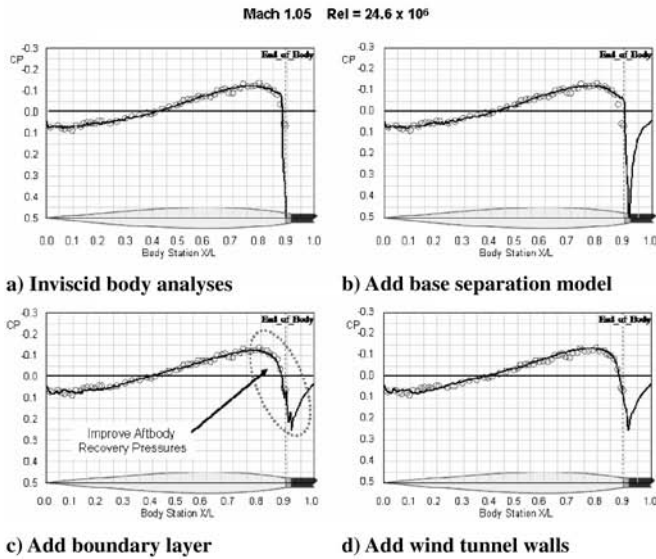
The theoretical predictions of pressure drag and total drag for subsonic through supersonic Mach numbers are compared with the experimental integrated pressure drags and total force balance drag measurements in Fig. 63 for the $X_{max}/L = 60\%$ body.

The inviscid pressure drag and total drag predictions obtained with the base wake simulation model are seen to agree quite well with the corresponding experimental results. The large discrepancy in the viscous drag predictions, including the wind-tunnel wall effects at $Mach 1.025$, are due to the sensitivity of the pressure drag on the $X_{max}/L = 60\%$ body to slight variations in the surface pressure distribution as previously shown in Figs. 59 and 60.



$X_{max}/L = 70\%$ Body Analyses Results

The $X_{max}/L = 70\%$ body has a rather sharp forebody and large aftbody slopes. The overall truncated body length is equal to 92.8% of the theoretical body length L . Inviscid predictions of the surface Mach number, pressure, and pressure drag distributions are



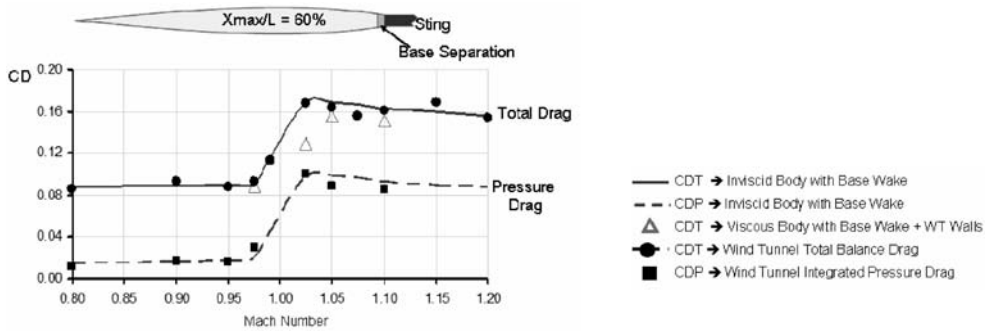


Fig. 63 $X_{max}/L = 60\%$ body drag variation with Mach number.

compared with test data in Fig. 64. The inviscid predictions were obtained with and without the aftbody base wake.

The flow over the body is fully subsonic for the freestream Mach numbers of 0.8 and 0.9. At Mach 0.95, a small region of supersonic flow occurs. At Mach 0.975, supersonic flow occurs over most of the aft end of the body which is terminated by a strong shock located just before the aftbody pressure recovery region.

Figure 65 contains near-field pressure and Mach number distributions around the body at a freestream Mach number of 0.975. The theoretical predictions correspond to inviscid free-air predictions. The large region of embedded supersonic flow is evident in the local Mach number contour plot. The near-field pressure distributions show that the effect of the aftbody base wake is restricted to the region close to the body axes.

The effects of the body boundary layer and the simulated wind-tunnel walls on the surface pressure coefficient and pressure drag distribution at Mach 0.975 are shown in Fig. 66. The free-air viscous analysis results compare very closely with experimental pressure distribution and the pressure drag distribution on the body.

The drag predictions obtained with the various analytical models are shown in Fig. 67. Once again, it is seen that the shape of the base separation wake has an important effect on the predicted pressure drag. The body boundary layer and wind-tunnel walls have little effect on the predicted pressure drag. The experimental pressure drag is slightly less than predicted because of the scatter in the test pressure data.

The overall experimental drag, however, is less than the predictions. This is believed to be the result of the experimental

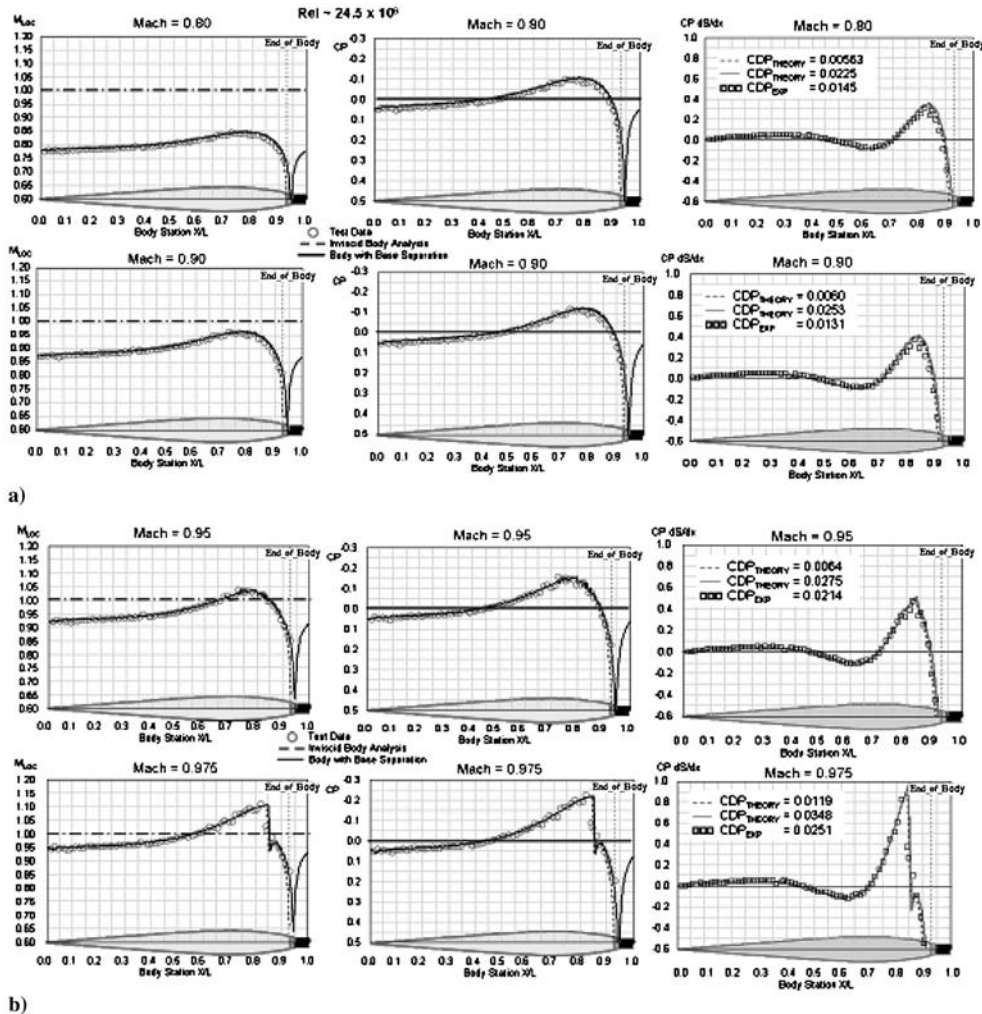


Fig. 64 Body surface Mach number, pressure, and pressure drag distributions at subsonic speeds.

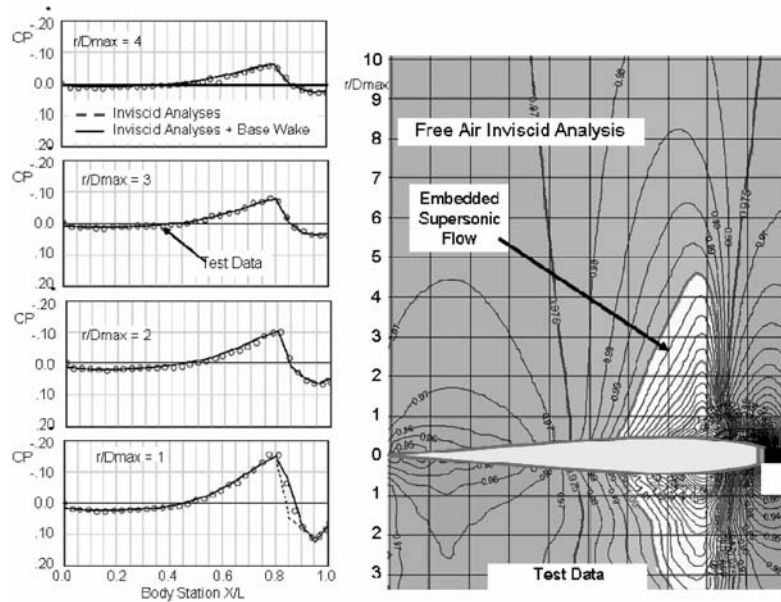


Fig. 65 Near-field pressure and local Mach number distributions for Mach 0.975.

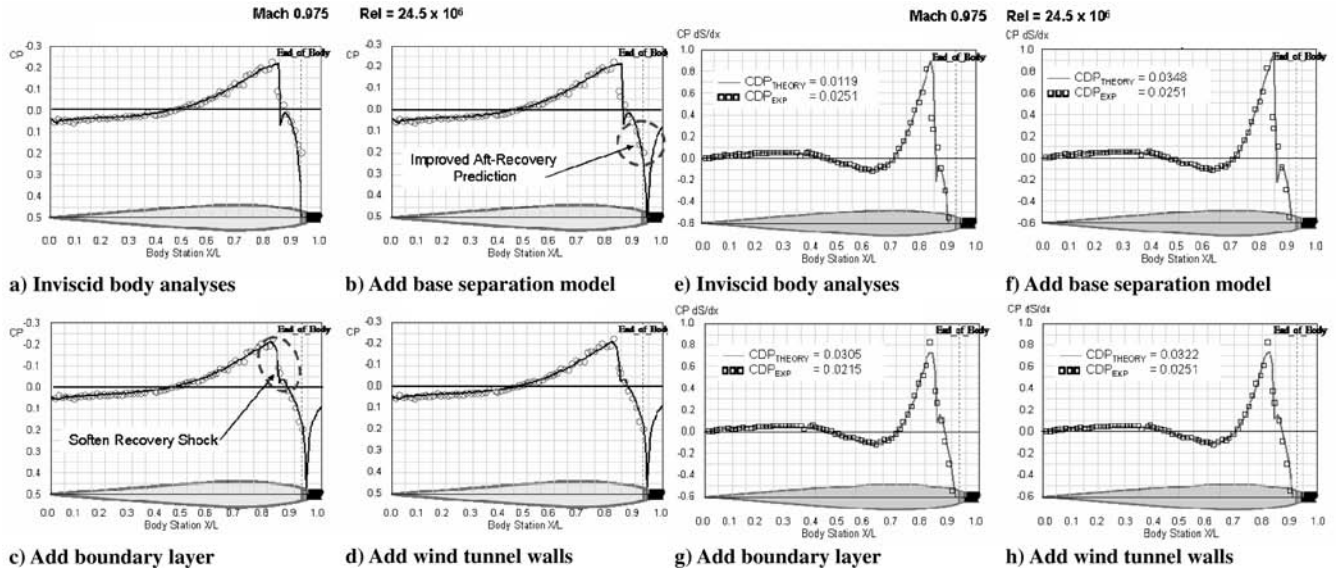


Fig. 66 Effect of boundary layer and wind-tunnel wall interference body CP and pressure drag.

viscous drag being less than the corresponding theoretical viscous drag predictions.

The results of Mach = 1.025 pressure distribution predictions obtained with the various analytical models are shown in Fig. 68. The

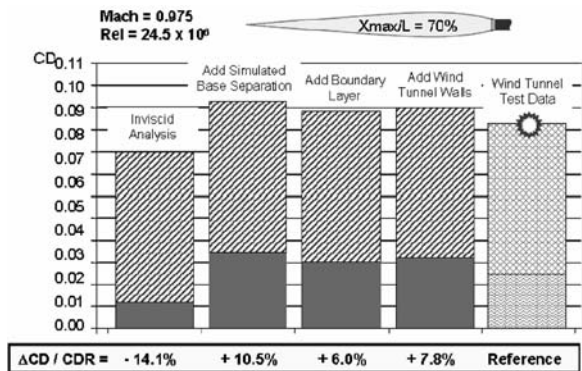


Fig. 67 Effect of analytical model on predicted drag.

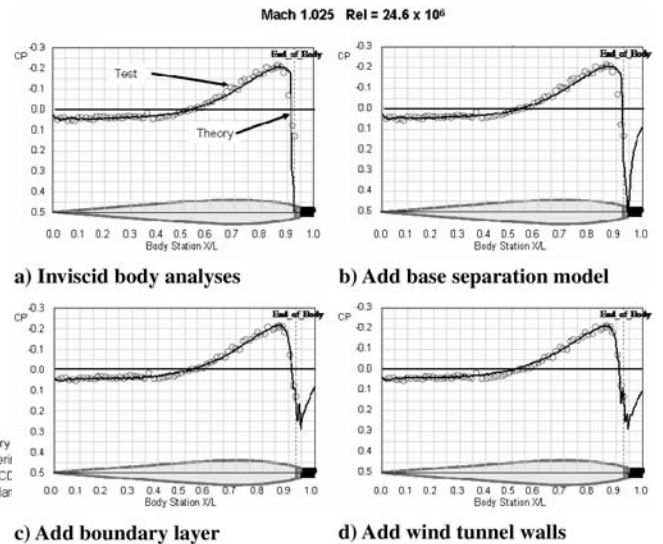


Fig. 68 Body pressure predictions.

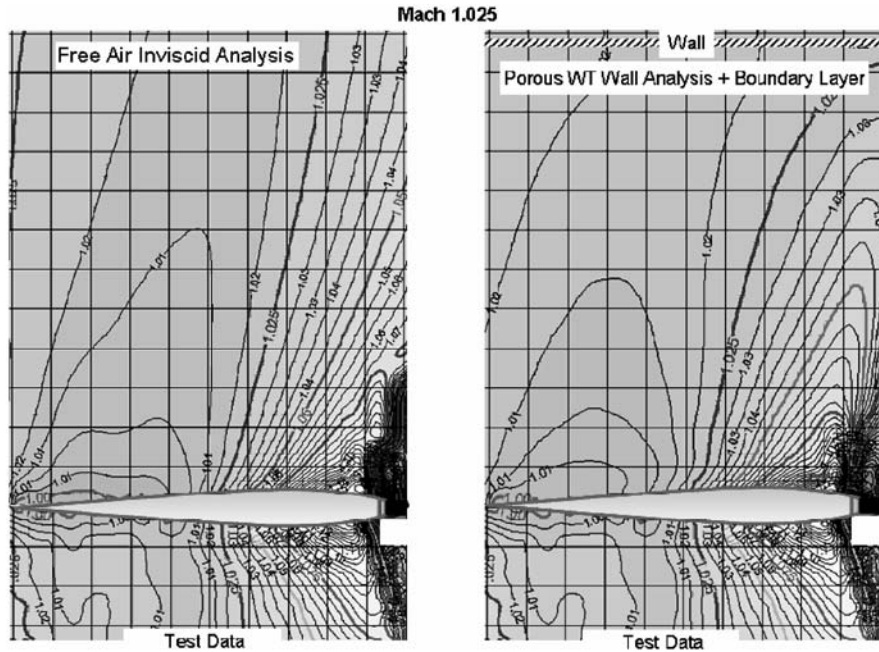


Fig. 69 Free-air vs wind-tunnel near-field local Mach number distributions.

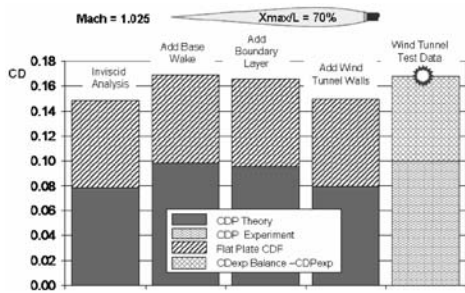


Fig. 70 Mach = 1.025 drag prediction comparisons for the $X_{max}/L = 70\%$ body.

inviscid predictions appear to agree well with the test data. The presence of the boundary layer clearly improved the aftbody recovery pressure distribution.

The free-air inviscid and viscous wind-tunnel near-field local Mach number predictions for a freestream Mach number of 1.025

are compared with test data in Fig. 69. The flow over the entire body is seen to be fully supersonic. The boundary layer and the wind-tunnel walls appear to have little effect on the local flowfield characteristics.

The pressure drag and total drag predictions obtained with the various analytical methods are shown in Fig. 70. Inviscid and viscous free-air predictions agree well with the test data. The viscous pressure drag prediction is less than the test data even though the differences in the corresponding pressure distributions (Fig. 68) are hardly discernible.

Results of similar analyses at Mach 1.05 and Mach 1.10 are shown in Figs. 71 and 72. It is seen that all of the viscous and inviscid predictions are essentially the same and agree with the test data.

Inviscid free-air and viscous wind-tunnel predictions of the near-field local Mach number distributions are compared with experimental results in Fig. 73. There is very little difference between the free-air predictions, the wind-tunnel predictions, and the test results.

Theoretical pressure drag and total drag predictions are compared with test data for subsonic through supersonic Mach numbers in

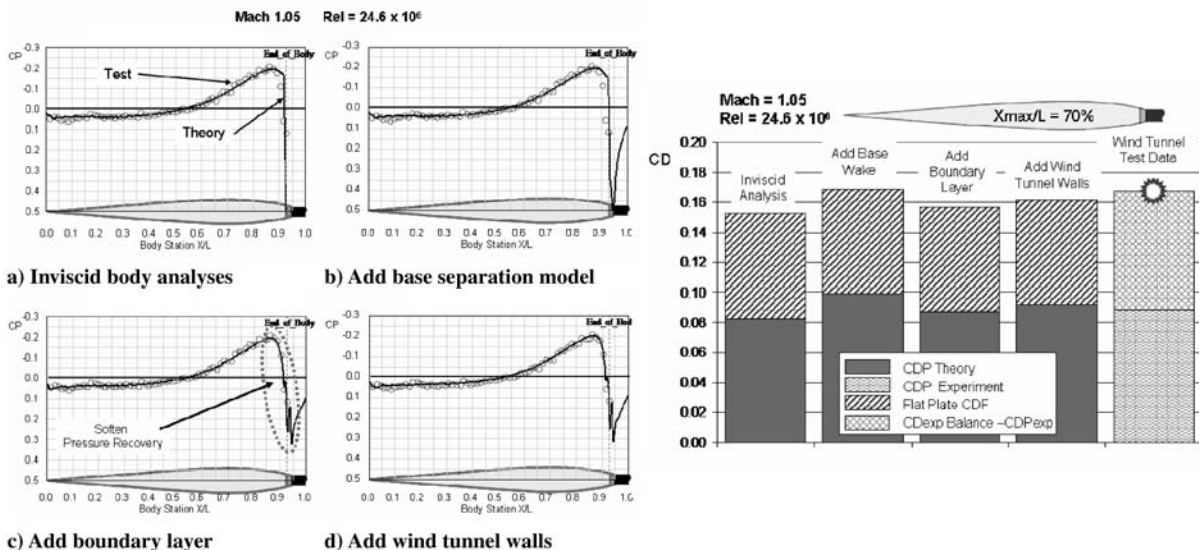


Fig. 71 Mach = 1.05 drag prediction comparisons for the $X_{max}/L = 70\%$ body.

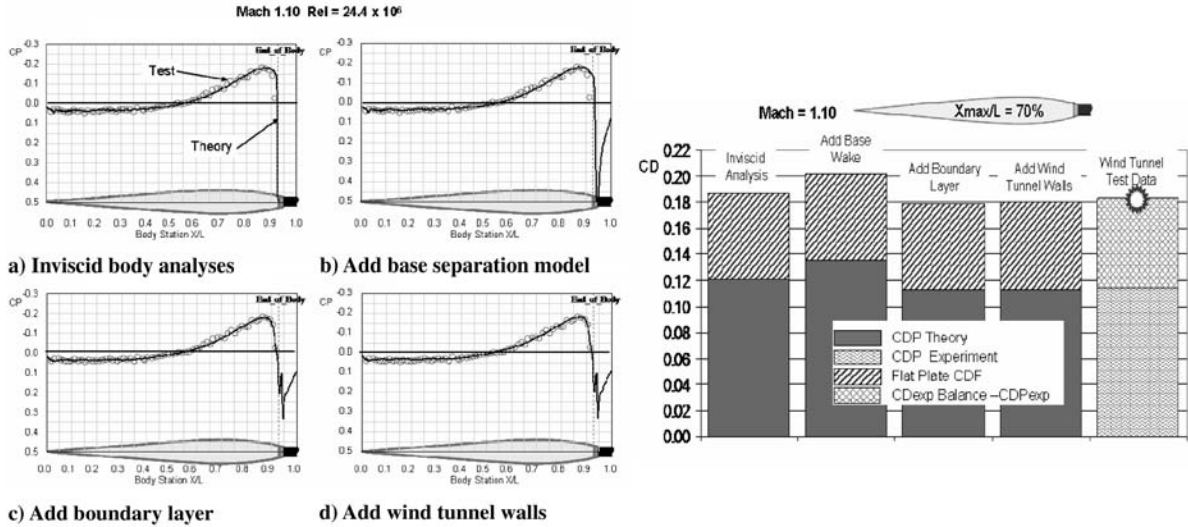


Fig. 72 Mach = 1.10 drag prediction comparisons for the $X_{max}/L = 70\%$ body.

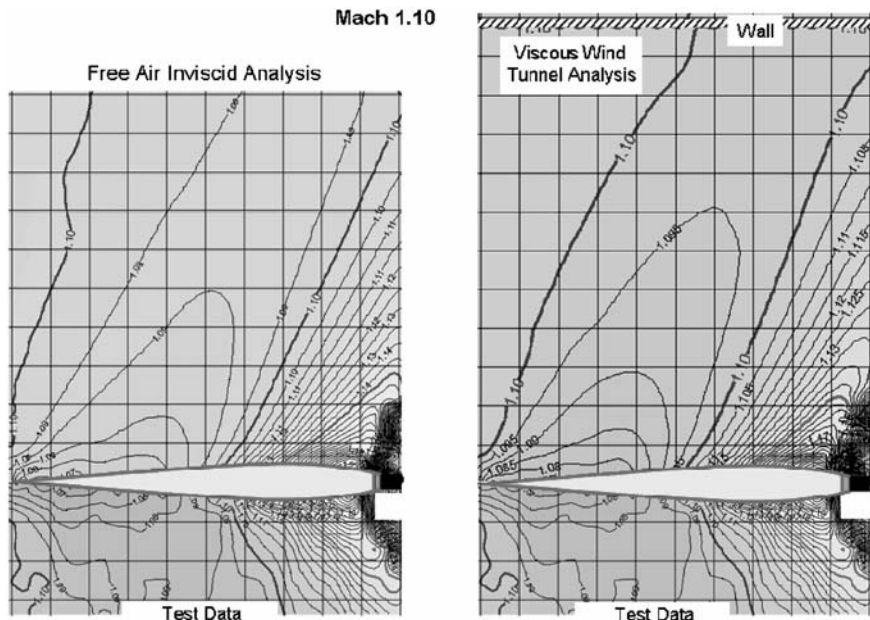


Fig. 73 Local Mach number distribution comparisons for the $X_{max}/L = 70\%$ body.

Fig. 74. The predictions agree well with the test data. The overall results of the analyses of the $X_{max}/L = 70\%$ body indicate that the shape of the body with the aft location of the maximum area results in very little wind-tunnel interference effects.

Body Shape Effects

The effect of the shape of the body, as defined by the location of the maximum radius station, on the local flow characteristics at the supercritical condition of Mach = 0.975 is shown in Fig. 75 as

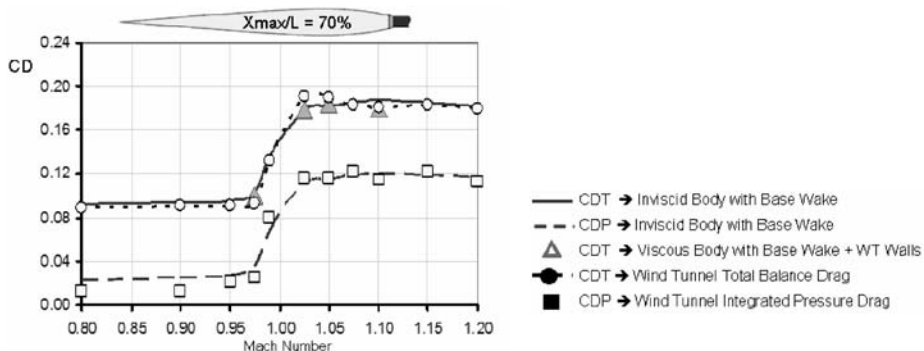


Fig. 74 Theoretical and experimental drag comparisons.

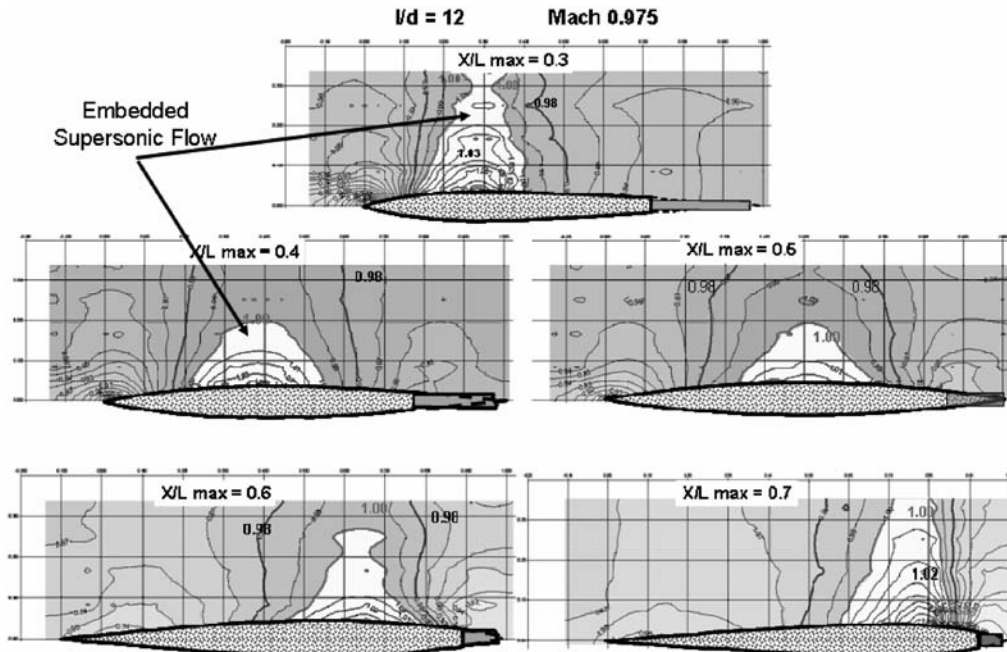


Fig. 75 Effect of body shape on local Mach number distribution.

flowfield Mach number distributions. For each of the body geometries, the region of embedded supersonic flow is typically centered around the maximum diameter station. The radial extent of the supercritical flow region increases significantly as the maximum diameter station moves either toward the forward or the aft ends of the body.

The shape of the body, as defined by the location of the maximum thickness, has a significant effect on the distribution and the magnitude of the pressure drag. An example is shown in Fig. 76 for a low supersonic Mach number of 1.025. The dashed lines in the figures correspond to the overall average pressure drag for each of the bodies. As previously mentioned, the average drag is the small difference between very large drag and very large thrust contributions. The nose region is the primary contributor of the wave drag for the $X_{max}/L = 30\%$ body. The aft end is the primary

contributor of the wave drag for the $X_{max}/L = 60\%$ and 70% bodies. For this example, it is seen that the body pressure drag varied by as much as 50% depending on the body shape.

One of the most significant findings of the current study is shown in Fig. 77. This figure shows the very significant effect of neglecting the shape of the aftbody separation wake shape on the overall drag predictions for a truncated body of revolution. It is seen that neglecting the aftbody wake effects can result in underprediction of the total body drag by 5–25% of the total body drag depending upon the body geometry and the freestream Mach number.

Conclusions (UFD)

The results of this study show that it is important to account for the effect of the flow separating from the aft end of the body and

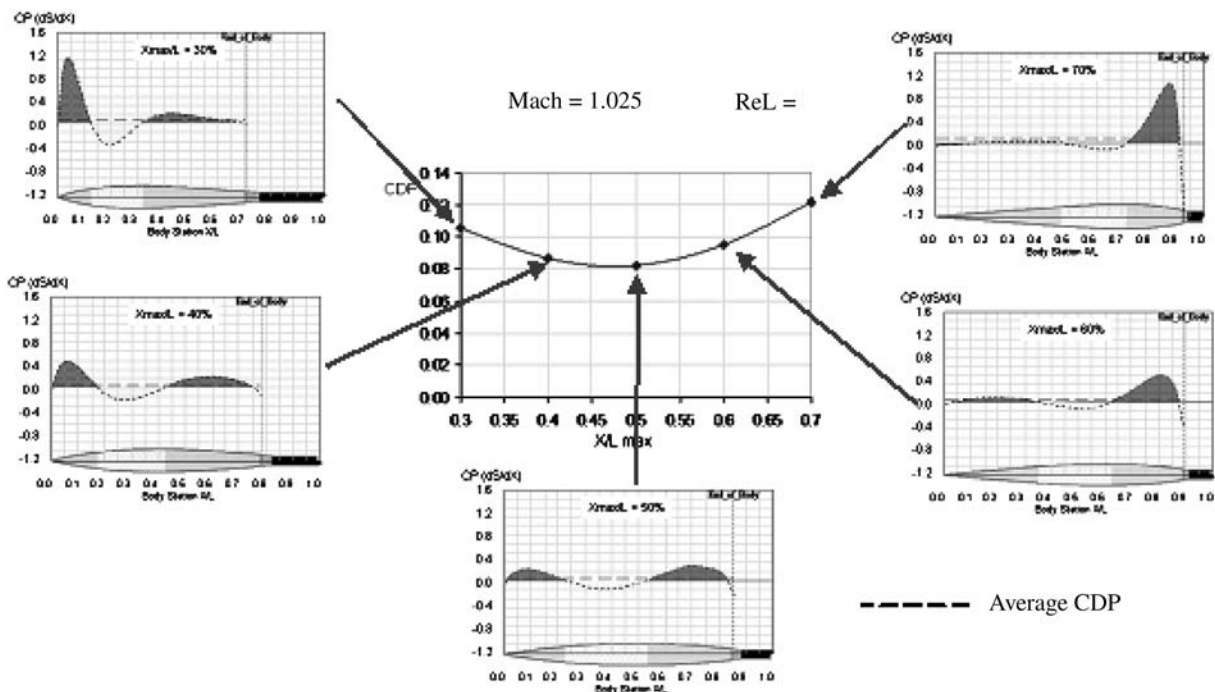


Fig. 76 Effect of body shape on sectional pressure drag.

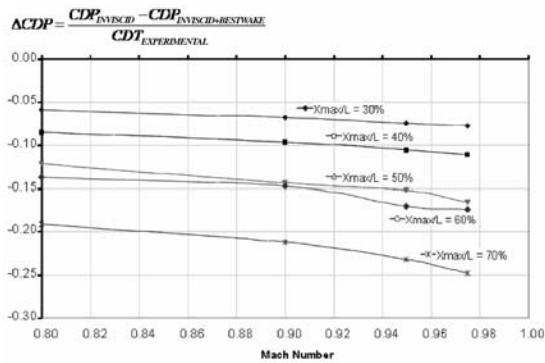


Fig. 77 Effect on total drag prediction because of not modeling the aftbody separation wake.

attaching to the sting for sting-mount wind-tunnel models at subsonic through low supersonic flow conditions. The aftbody base wake flow has an important effect on the aftbody recovery pressures and, consequently, on net pressure drag and total drag predictions. Flow predictions that do not account for this effect may significantly underpredict total body drag by 5–25% depending on the Mach number and body geometry.

The net pressure drag on the study configurations show that the net pressure drag is the result of two very large force components of local thrust and local drag. Consequently, the net pressure drag is very sensitive to small local changes in the surface pressure distributions.

Inviscid pressure distributions and pressure drag predictions, obtained with the base wake model, agreed well with the experimental data whenever the flow over a body was either fully subsonic or fully supersonic.

The primary effects of the boundary layer, depending upon the geometry and Mach number, included softening and slight forward movement of body shocks ($X_{\max}/L = 30\%$ and $X_{\max}/L = 40\%$ bodies) or softening the aftbody recovery gradients ($X_{\max}/L = 60\%$ and $X_{\max}/L = 70\%$ bodies).

Accounting for the boundary layer and for the wind-tunnel wall effects at near-sonic Mach numbers typically improved the test vs theory comparisons of the surface pressure distributions. However the effects on drag were generally small compared with the influence of the aftbody flow on the total drag.

The $X_{\max}/L = 30$ and 40% bodies displayed the most significant wind-tunnel interference effects at the lower supersonic Mach numbers. These geometries with greater forebody slopes and forward locations of the maximum area have detached nose shocks followed by large regions of embedded subsonic flow. This creates more significant forward disturbances with greater opportunity to reflect off the wind-tunnel walls and influence the flow features in the vicinity of the aft body.

The $X_{\max}/L = 60$ and 70% bodies with the far aft location of the maximum area stations demonstrated very little wind-tunnel interference effects for any of the subsonic through supersonic test Mach numbers. These bodies had essentially attached nose shocks for the lower supersonic Mach numbers.

The theoretical predictions of the wind-tunnel wall interference effects were obtained with an approximate representation of the wind tunnel as an equivalent porous wall circular test section. The predicted wall interference effects were therefore not in exact agreement with the test data. However if the theory predicted the existence of wall interference effects, then the test data did indeed indicate that the wind tunnel did not produce a free-air environment. In addition, the theory did identify the general effects of the wind-tunnel interference on the body pressures distributions and on the local near-field flow conditions.

The study results discussed in this paper demonstrated the value of using existing and even rather historic experimental data. The experimental data used in the current studies were obtained from NACA wind-tunnel tests conducted in approximately 1958.

References

- [1] Taylor, R. A., and McDevitt, J. B., "Pressure Distributions at Transonic Speeds for Parabolic-Arc Bodies of Revolution Having Fineness Ratios of 10, 12, and 14," NACA TN-4234, March 1958.
- [2] Taylor, R. A., and McDevitt, J. B., "Pressure Distributions at Transonic Speeds for Slender Bodies Having Various Axial Locations of Maximum Diameter," NACA TN-4280, July 1958.
- [3] Ashley, H., and Landahl, M., *Aerodynamics of Wings and Bodies*, Addison-Wesley, Reading, MA, 1965, pp. 107–110.
- [4] Langhans, R. A., and Flechner, S. G., "Wind-Tunnel Investigation at Mach Numbers from 0.25 to 1.01 of a Transport Configuration Designed to Cruise at Near-Sonic Speeds," NASA TM-X-2622, Aug. 1972.
- [5] Goodmanson, L. T., "Transonic Transports," Society of Automotive Engineers Paper 7102762, June 1971.
- [6] Williams, B., "Advanced Technology Transport Configuration Development," AIAA 72-756, Aug. 1972.
- [7] Bussoletti, J. E., Johnson, F. T., Bieterman, M. B., Melvin, R. G., Young, D. P., and Drela, M., "TRANAIR: Solution Adaptive CFD Modeling for Complex 3D Configurations," *Proceedings of the 1993 European Forum: Recent Developments and Applications in Aeronautical CFD*, Royal Aeronautical Society, Sept. 1993, pp. 10.1–10.14.
- [8] Bieterman, M. B., Bussoletti, J. E., Hilmes, C. L., Johnson, F. T., Melvin, R. G., and Young, D. P., "Adaptive Grid Method for Analysis of 3D Aircraft Configurations," *Computer Methods in Applied Mechanics and Engineering*, Vol. 101, 1992, pp. 225–249.
- [9] Drela, M., "Two-Dimensional Transonic Aerodynamic Design and Analysis Using the Euler Equations," Ph.D. Dissertation, Massachusetts Inst. of Technology, Gas Turbine Lab., Rept. 187, Cambridge, MA, Feb. 1986.
- [10] Drela, M., "Integral Boundary Layer Formulation for Blunt Trailing Edges," AIAA Paper 89-2200, Aug. 1989.
- [11] Wilcox, D. C., *Turbulence Modeling for CFD*, DCW Industries, La Canada, CA, Nov. 1988, p. 3.
- [12] Chang, P. K., *Separation of Flow*, Pergamon, New York, 1970, pp. 278–280.
- [13] Kulfan, R. M., "Historic Background on Flat Plate Turbulent Flow Skin Friction and Boundary Layer Growth," *1998 NASA High-Speed Research Program Aerodynamic Performance Workshop*, Vol. 1, Pt. 1, NASA CP-1999-209692, Dec. 1999, pp. 477–513.
- [14] Kulfan, B. M., "Assessment of CFD Predictions of Viscous Drag," AIAA Paper 2000-2391, 21 June 2000.